UNIVERSITÀ DEGLI STUDI DI PADOVA

Dipartimento di Fisica e Astronomia "Galileo Galilei"

Master Degree in Physics

Final Dissertation

In-beam commissioning of the AGATA-PRISMA setup at Legnaro National Laboratories

Thesis supervisors

Prof. Daniele Mengoni

Dott. Franco Galtarossa

Candidate

Dott. Elia Pilotto

Academic Year 2021/2022

Abstract

In the field of high-resolution gamma-ray spectroscopy, the impressive technological advancements of the last few decades have been one of the keys to push further the boundaries of nuclear research. In this context, the coupling of modern large-acceptance magnetic spectrometers to new-generation large gamma arrays for particle-gamma coincident measurements will enable new insight in the study of the nuclear structure near the valley of beta-stability. At the Legnaro National Laboratories (LNL), INFN, the large acceptance magnetic spectrometer PRISMA has been recently coupled to the Advanced GAmma-ray Tracking Array (AGATA), a device built from a European collaboration, that currently represents the state of the art in gamma-ray detection. Such a setup is very well suited for the study of Multi-Nucleon Transfer (MNT) reactions with high intensity stable beams. These populate a number of moderately exotic channels with relatively high cross sections, allowing to study the structure of many nuclei in the same experiment. The experiments largely benefit of the high selectivity for the identification of the transfer channel as well as the measurement of the recoil velocity vector on an event-by-event basis. A first in-beam commissioning has been carried out to evaluate the capabilities of the complete setup. In this thesis, the evaluation of the performance of the AGATA-PRISMA setup is carried out. To this aim, the data from a MNT reaction ^{32}S + ^{124}Sn at 160 MeV employing a 0.5 mg/cm^2 thick target, corresponding to 35 hours of total beam time, have been processed and analyzed.

The thesis work mostly focuses on the PRISMA data processing and standalone performance evaluation. A localized loss of efficiency was observed in the position distribution recorded by the Micro-Channel Plate (MCP) entrance detector, matching the observations of previous experimental campaigns. The performance of the Ionization Chamber (IC) of the spectrometer after the refurbishment of the electronics and VME read-out system was evaluated in terms of atomic number resolution and good operation of the different elements. A comparison between different methods for the calibration of the IC using either a charge injector or a fine tuning of the parameters was carried out. Distinctive structures were observed in the $\Delta E - E$ matrices produced using single columns of electrodes of the IC and were associated to different charge states and atomic numbers, suggesting the possibility to use the technique to monitor the population of transfer channels during an experiment. The mass spectrum of the recoils was determined through trajectory reconstruction and charge state identification and the corresponding resolution of the apparatus was quantified. Partial efficiencies were extracted for various sensitive components of the spectrometer, revealing potential issues with the timing signals produced by the MCP entrance detector. Finally, the sustainable rate capability of the device was verified.

Afterwards, the quality of the Doppler correction and the reconstruction of the Total Kinetic Energy Loss (TKEL) were evaluated. The time coincidence between the the magnetic spectrometer and the gamma-ray tracking array was verified and the background was reduced through a refined time window. Doppler correction of the gamma-ray energies was performed for both beam-like and target-like binary partners of the reaction, taking into account the energy loss in the target and the kinematic reconstruction of the interaction to obtain the velocity vector of the heavier recoils. The resolution of the setup in the Doppler-corrected spectra was evaluated in a wide range of energies, suited for discrete high-resolution spectroscopy. A condition on the TKEL parameter was applied for the ^{33}S products to verify the ability to discriminate between transitions originating from high-lying or low-lying excited states. This technique will find application in future experiments, in particular in the measurement of the lifetime of nuclear excited states, to control the entry point of the reaction and

limit the contribution of undesired feeding transitions to the state of interest.

Riassunto

Nel campo della Fisica Nucleare, la spettroscopia ad alta risoluzione dei raggi gamma è uno degli strumenti più utilizzati per indagare la struttura del nucleo atomico. Tali studi permettono di misurare osservabili fondamentali dei livelli energetici dei nuclei, quali energia, spin-parità e probabilità di transizione, e confrontarli con le predizioni dei modelli teorici di struttura nucleare. Negli ultimi decenni, gli avanzamenti tecnologici nella rivelazione di raggi gamma sono stati considerevoli, permettendo lo studio di sezioni d'urto di diversi ordini di grandezza inferiori a quanto possibile in precedenza. Ai Laboratori Nazionali di Legnaro (LNL) dell'INFN, lo spettrometro magnetico a grande accettanza PRISMA è stato recentemente accoppiato all'Advanced GAmma Tracking Array (AGATA), uno strumento frutto di una collaborazione Europea, stato dell'arte nella rivelazione dei raggi gamma. Il setup è considerato particolarmente adatto per lo studio di reazioni di trasferimento di molti nucleoni (MNT) poco al di sopra della barriera coulombiana, in esperimenti con fasci stabili ad alta intensità. Tali interazioni popolano un grande numero di canali moderatamente esotici con sezioni d'urto di trasferimento considerevoli. Ciò permette di investigare in un solo esperimento la struttura di diversi nuclei posizionati nei dintorni della valle di stabilità. L'alta selettività del setup è ottenuta tramite l'identificazione dei prodotti di reazione e la determinazione, evento per evento, del loro vettore di velocità. Tali caratteristiche svolgono un ruolo di fondamentale importanza per lo studio di questa categoria di reazioni. Questo lavoro di tesi si pone come obiettivo una valutazione accurata delle performance del setup AGATA-PRISMA, nel suo primo esperimento di commissioning sotto fascio. A tal scopo, sono stati analizzati i dati associati alla reazione di MNT $^{32}\mathrm{S} + ^{124}\mathrm{Sn}$ a 160 MeV con target di 0.5 mg/cm^2, relativi ad un totale di 35 ore di acquisizione.

Nel corso di questo lavoro, particolare attenzione è stata riservata al processing dei dati di PRISMA e alla valutazione delle sue performance come strumento a sé stante. Una regione a bassa efficienza è stata osservata nella distribuzione delle posizioni misurate dal Micro-Channel Plate (MCP) detector, in accordo con osservazioni provenienti da scorse campagne sperimentali. Le performance della camera di ionizzazione (IC) dello spettrometro sono state valutate in seguito al completo rinnovo dell'elettronica e del sistema di read-out VME, in termini di risoluzione nell'identificazione del numero atomico e del corretto funzionamento delle varie componenti dello strumento. Si è in eseguito un confronto fra diversi metodi di calibrazione della IC utilizzando un iniettore di carica o un fine tuning dei parametri. Particolari strutture distintive sono state osservate nelle matrici $E - \Delta E$ costruite usando singole colonne della IC. Queste sono poi state associate ai diversi stati di carica e numeri di massa atomica dei prodotti di reazione, suggerendo la possibilità di sfruttare questa tecnica al fine di monitorare il popolamento dei canali di trasferimento durante l'analisi on-line dell'esperimento. Lo spettro di massa dei nuclei rilevati è stato ottenuto tramite ricostruzione della traiettoria e identificazione del loro stato di carica e la corrispondente risoluzione in massa dell'apparato è stata quindi quantificata. Efficienze parziali sono inoltre state stimate per alcune delle componenti sensibili dello spettrometro magnetico, rivelando la presenza di potenziali perdite di statistica causate del segnale di tempo prodotto dal rivelatore MCP. Infine, sono state verificate le capacità dell'apparato in termini di dead time e rate di acquisizione.

Ci si è in seguito focalizzati sulla valutazione delle performance del setup in termini di correzione Doppler e stima della perdita totale di energia cinetica (TKEL). Si è dapprima verificata la coincidenza fra i due strumenti e in seguito ridotto il background utilizzando una ristretta finestra temporale. La correzione Doppler delle energie dei raggi gamma è stata eseguita per entrambi i prodotti di reazione,

sia beam-like che target-like, tenendo conto della perdita di energia nel materiale del bersaglio e della ricostruzione cinematica dell'interazione, al fine di ottenere il vettore velocità dei nuclei più pesanti. La risoluzione del setup negli spettri gamma a seguito della correzione Doppler è stata calcolata nel range di energie tipico di questi studi di spettroscopia gamma. Una selezione del parametro di TKEL è stata implementata per lo spettro gamma relativo al ^{33}S, al fine di verificare le capacità di distinguere transizioni gamma originate da stati ad alta o bassa energia di eccitazione. Tale tecnica troverà ampio utilizzo in futuri esperimenti dedicati alla misura di vite medie di stati nucleari eccitati, dove può essere utilizzata per limitare il contributo di transizioni provenienti da stati che decadono gamma sullo stato di interesse.

Contents

Chapter 1

Introduction

1.1 Motivation of the thesis

High-resolution gamma-ray spectroscopy is an essential tool in experimental nuclear physics to investigate the structure of the atomic nucleus, as most of its bound excited states decay by emitting gamma radiation. The technique allows to measure fundamental observables of nuclear excited states such as energy, spin-parity and transition probability, which can be compared with the predictions of nuclear structure theoretical models. During the last few decades the technological advancements in the field have been remarkable, starting with the advent of Compton suppressed high purity Germanium (HPGe) arrays, such as Gammasphere [1] and Euroball [2], which allowed an increase in sensitivity by 2-3 orders of magnitude in the span of $10 - 20$ years. The current state of the art in high resolution gamma-ray spectroscopy, however, is represented by highly segmented HPGe arrays, which further improve the previous figure by another $10^2 - 10^3$ factor. At the moment, only two such projects are active in the world: the Gamma-Ray Energy Tracking Array (GRETA) [3], located in the United States, and the European Advanced GAmma Tracking Array (AGATA) [4, 5]. The latter has been travelling through Europe, since 2009, to be employed at both stable and radioactive beam facilities, while being expanded and improved [6, 7, 8]. Most recently, the AGATA array has been installed at the INFN Legnaro National Laboratories (LNL) [9], where the apparatus has been coupled to the PRISMA large acceptance magnetic spectrometer [10] for the forthcoming experimental campaign.

The AGATA array presents a modular structure composed of highly segmented HPGe crystals that form an almost complete 4π shell around the target. A detailed description of the apparatus is reported in Section 2.2 of this work. HPGe detectors in general are the state of the art in terms of energy resolution for the detection of gamma rays. However, the innovative aspect of the technology is the possibility to use *Pulse Shape Analysis* algorithms to determine the position of the gamma-ray hits inside the crystals with a precision on the order of ~ 5 mm [4], which translates to an unprecedented angular resolution of about $\sim 1^\circ$. This allows to correct for localized neutron damage effects and represents the basis for the *Tracking* algorithm that reconstructs the path of the gamma rays inside the array. This procedure is able to significantly increase both the absolute efficiency and peak-to-total ratio of the apparatus, while the angular resolution is critical to perform a high-quality Doppler correction of the gamma-ray spectrum.

The large acceptance PRISMA magnetic spectrometer, on the other hand, has been developed at LNL in the early 2000s and has, since then, been employed successfully in a number of experimental campaigns. A detailed description of the apparatus is reported in Section 2.1 of this work. The spectrometer is composed of a number of elements, most noticeably dipole and quadrupole magnets, which perform the focusing and $B\rho$ separation of the ions, an MCP entrance and MWPPAC focal plane detectors, used for trajectory reconstruction and ToF measurement, and finally a segmented transverse-field ionization chamber for energy loss measurement. The device can rotate around the target in the angular range from -30° to +130° with respect to the beam axis, allowing for a great versatility of the apparatus. The main purpose of the spectrometer is to perform an event-by-event

identification of the nuclei produced in the reaction in mass number A and atomic number Z, along with the measurement of their velocity vector after the target. This is achieved through trajectory reconstruction combined with the identification provided by the ionization chamber used in $\Delta E - E$ configuration. The velocity vector of the recoils, which is critical for the kinematics reconstruction and the Doppler correction, is measured precisely on an event-by-event basis. The typical performance of the spectrometer are summarized in Table 2.1.

The coupling of the two apparatuses for coincidence measurements brings a number of advantages. The identification of the recoils in terms of atomic and mass numbers, performed by PRISMA, allows to easily select the channel of the reaction, thus drastically reducing the background. In addition, thanks to the measurement of the velocity and direction of motion, both Q-value estimation and a high-quality Doppler correction can be achieved. The use of the AGATA array in particular, with its unprecedented angular resolution and impressive energy resolution, absolute efficiency and peak-to-total ratio, allows to increase the sensitivity of the setup and therefore tackle the measurement of even tinier cross sections.

This setup is particularly suited for the study of *multi-nucleon transfer* (MNT) reactions (see Section 1.4 for a brief explanation). In such measurements PRISMA is set at the so-called *grazing angle*, where the transfer differential cross section is maximum. The ability of the spectrometer to perform event-by-event nuclear species identification is critical for this kind of experiments, where a large number of reaction channels are populated. MNT reactions are known to populate preferentially yrast and near-yrast excited states up to medium angular momentum ($\sim 8 - 10\ \hbar$), depending on the specific system and the bombarding energy. In this context, the superb angular resolution of the AGATA array, combined with the excellent angular resolution ($\sim 0.2^{\circ}$) for charged particles of the PRISMA entrance detector, leads to an outstanding quality of the Doppler correction which is crucial for in-beam gamma-ray spectroscopy experiments.

The objective of this thesis is to evaluate the performance of the setup in its first in-beam commissioning experiment, which employed the reaction below the Coulomb barrier $^{58}\mathrm{Ni} + {}^{197}\mathrm{Au}$ at 225 MeV and the MNT reaction $^{32}\mathrm{S} + {}^{124}\mathrm{Sn}$ at 160 MeV.

1.2 AGATA-PRISMA in-beam commissioning

The coupling of the AGATA array to the PRISMA magnetic spectrometer at the Legnaro National Laboratories has been the consequence of a strong interest by the scientific community, as proven by various Letters of Intents presented in a number of workshops [11]. Due to the complexity of the setup, a commissioning under realistic experimental conditions is required before the beginning of the forthcoming research campaign [12]. Moreover, both AGATA and PRISMA were subject to a number of interventions since their previous period of activity. A detailed description of the two apparatuses is reported in Chapter 2 of this work.

The AGATA array has been disassembled from the GANIL nuclear research centre (France) and relocated to the Legnaro National Laboratories (Italy). The movement of the apparatus between different facilities represents a critical moment in its life. Not only the Agata Triple Cluster modules (ATCs) are dismantled from their supporting structure, but they also have to be unbiased and their temperature raised to room conditions, potentially stressing the internal structure of the germanium crystals.

In regards to the PRISMA magnetic spectrometer, the delay lines of the Micro-Channel Plate (MCP) entrance detector have been replaced in order to recover an inefficient region of the device. In addition, both the front-end and back-end electronics of the PRISMA ionization chamber (IC) have been completely refurbished as all the preamplifiers and amplifiers have been replaced. 10 additional Time to Digital Converters (TDCs) have been installed to measure the vertical position of the ions from the time difference between the MWPPAC cathode signal and the IC anode signals. The data acquisition and VME readout systems have also been upgraded to reduce dead time and increase the maximum rate of acquisition.

The in-beam commissioning of the AGATA-PRISMA setup is designed to assess performance in realistic working conditions. The objectives of the experiment are:

- to evaluate the capabilities of the data acquisition system and software, in terms of quality of the AGATA-PRISMA coincidence, trigger and maximum rate.
- to gauge the performance of the AGATA Pulse Shape Analysis and Tracking, in terms of efficiency, energy resolution and peak-to-total ratio.
- to test the software for both on-line and near-line analysis, also in terms of maximum rate sustainable.
- to confirm the recovery of the full efficiency of the PRISMA MCP detector and check the performance of the new IC electronics and VME read-out system. To verify rate capacity and assess the ability to reconstruct the vertical position of the ions.
- to quantify atomic and mass number resolutions of the PRISMA magnetic spectrometer and verify the presence of potential efficiency losses.
- to judge the quality of the Doppler correction of prompt gamma rays, in terms of energy resolution and precision of the measurement, for both beam-like and target-like partners of the reaction.

This thesis will mainly focus on evaluating the performance of the PRISMA magnetic spectrometer as well as the quality of the final Doppler correction for both partners of the reaction. The work will also discuss the possibility to employ Total Kinetic Energy Loss (TKEL) selection to discriminate gamma-ray transitions originating from low-lying and high-lying states.

1.3 Heavy-ion reactions

Since the discovery of the atomic nucleus, at the beginning of the 20^{th} century, heavy-ion reactions have been an important tool in the investigation of the properties of the nuclear system and the validation of theoretical models in both Nuclear and Subnuclear Physics [13]. Complete quantum mechanical knowledge of the structure of the colliding many-body nuclear systems as well as the dynamics of the reaction are both in principle needed for a precise description of these processes. Nevertheless, a semiclassical approximation is in some cases sufficient to understand the main experimental properties of heavy-ion reactions. In this picture, considering the process $a + A \rightarrow B + b$, the real part of the radial effective potential of the interaction can be written as

$$\begin{aligned} V_{eff}(r) &= V_c(r) + V_n(r) + V_l(r) \\ &= \frac{Z_a Z_A e^2}{r} + \frac{V_0}{1 + \exp\left(r - (R_a + R_A)\right)/a} + \frac{l(l+1)\hbar^2}{2\mu r} \end{aligned} \tag{1.1}$$

where $R_i = 1.20 A_i^{1/3}$ fm is the radius of the two nuclei and $\mu = (A_a \cdot A_A)/(A_a + A_A)$ their reduced mass. The quantities $V_c(r)$, $V_n(r)$ and $V_l(r)$ represent the Coulomb and nuclear potential and the centrifugal barrier, respectively, with a Woods-Saxon parametrization for the nuclear potential.

The so called Coulomb barrier is defined as the maximum of the interaction potential in the assumption of head-on collisions ($l = 0$) and is therefore characterized by the relation

$$\frac{\partial V_{eff}(r)}{\partial r} = 0 \tag{1.2}$$

In most cases, the height of the Coulomb barrier can be approximated as

$$E_B = \frac{Z_a Z_A e^2}{r_C} \tag{1.3}$$

where $r_C = R_a + R_A = 1.20 \cdot (A_a^{1/3} + A_A^{1/3})$ fm is the sum of the radii of the two nuclei. The energy that is absorbed or released by the interaction between two ions is called Q value of the reaction and defined as

$$Q = T_f - T_i = (m_i - m_f)c^2 \tag{1.4}$$

where T_f, T_i are the total kinetic energies of the system before and after the interaction, respectively, and m_f, m_i the masses of the corresponding nuclei. If the reaction products are generated in excited states, the final Q value will be the difference between the ground-to-ground-state Q value Q_{gs} and the total excitation energy E_{ex}.

$$Q = Q_{gs} - E_{ex} \tag{1.5}$$

Finally, the Total Kinetic Energy Loss (TKEL) of the reaction can be defined as the opposite of the Q value.

When the energy of the collision, in the center of mass frame of reference, is just above the Coulomb barrier, various kinds of reactions take place depending on a number of parameters, such as the collision time, the transferred angular momentum and the impact parameter. The latter represents the perpendicular distance between the path of the projectile and a complete head-on trajectory when the two nuclei are still far from each other. With the increase of the impact parameter, the reaction evolves from a central collision, namely fusion and deep inelastic scattering, to a more peripheral interaction, in order quasi-elastic grazing-type reaction, Coulomb excitation and elastic scattering.

1.4 Multi-nucleon transfer reactions

Processes in which few nucleons are transferred between target and projectile occur with maximum probability when the distance of closest approach of the ions is comparable to the sum of their two radii and the tails of their wave functions start to overlap [14, 15]. These grazing-type conditions take place in peripheral collisions for a very limited range of scattering angles. As a consequence, the differential cross section of *transfer reactions* presents a bell-shaped angular distribution with a maximum at a certain *grazing angle*. This is determined mainly by the nature of the two nuclei as well as the energy of the collision and can be successfully inferred through semiclassical estimations.

Transfer reactions play an essential role in heavy-ion collision studies for both reaction dynamics and nuclear structure. These processes occur at the surface of the two nuclei and are mediated by both the nuclear and Coulomb fields. They are classified as *direct reactions*, meaning that their collision time is usually very short ($10^{-22} - 10^{-23}$ s) with respect to compound-nucleus formations ($10^{-16} - 10^{-18}$ s), such as fusion reactions. In addition, at energies near the Coulomb barrier, transfer reactions are one of the main causes for the loss of flux in the elastic channel. In these processes, very little change between initial and final states of the two nuclei is observed, as they occur due to the interaction with a specific degree of freedom, either of a single nucleon or a collective coordinate.

Multi-nucleon transfer reactions (MNT) represent a subgroup of transfer reactions located in between quasi-elastic interactions and deep inelastic scattering, both in terms of collision time and energy loss. As such, they play a very important role in the evolution of the reaction mechanism between the two regimes. More specifically, as the number of transferred nucleons increases, the reaction shifts from the quasi-elastic to the deep inelastic character.

The amount of energy typically dissipated in MNT reaction can be estimated using a very simple yet insightful model [15]. In heavy-ion interactions the number of independent single-particle transfer

channels is very large ($N \sim 100$), therefore, at a first order approximation, the same probability p can be assigned to each of them. Under this assumptions, the probability of transferring n particles is given by the binomial distribution:

$$P_n = \binom{N}{n} p^n (1-p)^{N-n} \tag{1.6}$$

The average number of transferred nucleons is thus $\langle n \rangle = pN$ and the corresponding energy loss $\langle E_{loss} \rangle = \langle n \rangle Q$. In heavy-ion collisions, $Q = 5$ MeV can be taken as a typical value for the average energy loss in each transition and 10 as the average number of transferred nucleons, yielding a Total Kinetic Energy Loss (TKEL) for the transfer process on the order of 50 MeV, in agreement with experimental distributions. Moreover, this result indicates that in MNT experiments the exchange of many nucleons may represent the main cause for the dissipation of energy.

In general, MNT reactions between stable projectiles and targets tend to populate a wide variety of moderately exotic nuclei with relatively large cross sections, of the order of few to tens of mb for the less exotic channels. As a consequence, in the latest decades, MNT reactions have been increasingly employed to investigate the nuclear structure near the valley of beta stability. This line of research has recently become more viable thanks to the advent of modern large acceptance magnetic spectrometer, namely PRISMA [10] at INFN-LNL [9], MAGNEX [16] at INFN-LNS [17] and VAMOS [18] at GANIL [19]. These devices provide a larger efficiency with respect to the previous generation by more than one order of magnitude [15].

One last important consideration regarding MNT reactions is the role of the so called *optimum Q-value* Q_{opt} in the determination of the cross section of the different transfer channels. This quantity is obtained through semiclassical calculations by requiring that the trajectories of the two nuclei match smoothly at the point of the interaction. It can be proven that the probability of populating a specific channel is maximized in such conditions and falls off relatively quickly in a bell-shaped curve when the Q value of the reaction is different from Q_{opt}. Due to the effect of the Coulomb interaction, the quantity is mainly dependent on the atomic number of the ions [20] and can be approximated to

$$Q_{opt} \simeq E_{beam} \left(\frac{Z_b Z_B}{Z_a Z_A} - 1 \right) \tag{1.7}$$

As a result, proton stripping typically presents a distinctively negative Q_{opt}, while proton pick-up shows a positive one. Neutron transfer reactions, on the other hand, have an optimum Q-value that is close to zero, with neutron stripping being slightly shifted towards the negative side and neutron pick up towards the positive one. Still, the resulting distribution has to be convoluted with the range of possible Q-values accessible in the interaction. Figure 1.1 shows the result of such operation both theoretically, in the reaction ^{58}Ni + ^{208}Pb at 330 MeV, and experimentally, for ^{40}Ca + ^{208}Pb at 235 MeV. The proton pick up and neutron stripping channels are clearly suppressed due to the effect of the optimum Q-value. This behaviour is replicated in the ^{32}S + ^{124}Sn reaction that is at the focus of this thesis.

Accurate predictions of transfer cross sections in MNT reactions can be obtained using the semiclassical model GRAZING [21, 22, 23]. The code calculates the evolution of the reaction by taking into account, besides the relative motion variables, the intrinsic degrees of freedom of projectile and target. These correspond to surface degrees of freedom and one-nucleon transfer channels. The relative motion of the system is calculated in a nuclear plus Coulomb effective field. The exchange of many nucleons proceeds via a multi-step mechanism of single nucleons. This model has been successfully applied for the description of multi-nucleon transfer reactions as well as fusion reactions and barrier distributions.

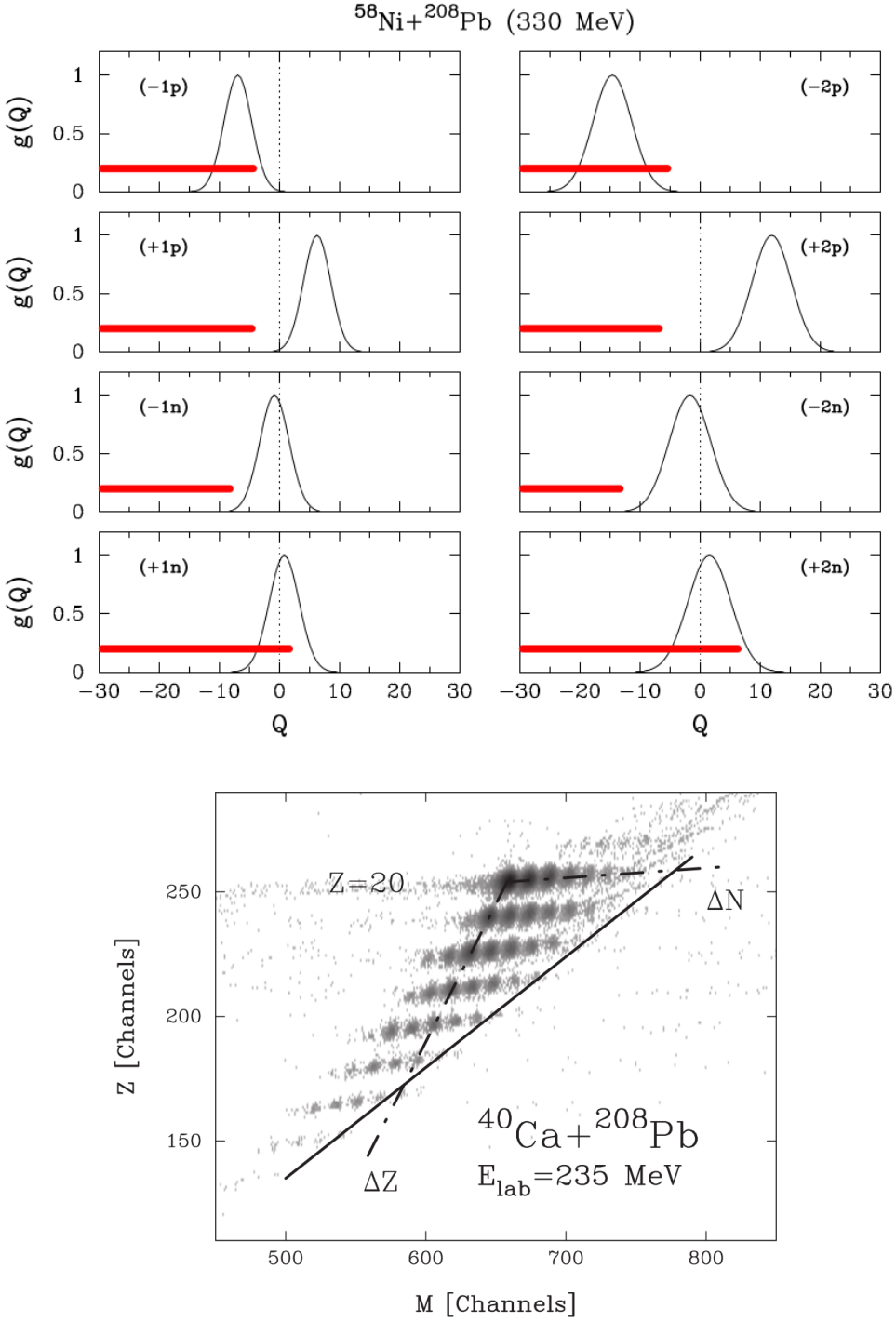

Figure 1.1: (Top) Adiabatic cut-off functions for one- and two-neutron and proton transfer channels for the reaction $^{58}\mathrm{Ni} + {}^{208}\mathrm{Pb}$ at 330 MeV. The Q-value (on the x axis) is expressed in MeV. The horizontal line represents the location of all possible transitions, extending up to the ground-to-ground-state Q value. Taken from reference [15]. (Bottom) Mass-charge distribution of the Ca-like products in the $^{40}\mathrm{Ca} + {}^{208}\mathrm{Pb}$ reaction at 235 MeV. Taken from reference [24].

1.5 Doppler correction

As anticipated in Section 1.1, the combination of large acceptance magnetic spectrometers and gamma arrays represents a powerful tool in modern gamma-ray spectroscopy experiments. The identification and trajectory reconstruction of the reaction products, however, requires the recoils to leave the target with a reasonable amount of kinetic energy in order to be detected in the spectrometer and trigger

an event. As a consequence, relatively thin targets have to be employed while the vast majority of gamma-ray production takes place in flight. In many cases, this notion is true also for the target-like partner of the reaction, which receives enough momentum to leave the target before its decay. As an example, in the experiment discussed in this thesis, a ^{124}Sn target of 0.5 mg/cm^2 tilted by 35° was employed. The average velocity of the beam-like and target-like reaction products can be approximated to about 9% and 2% of the speed of light, respectively. This translates to a time spent inside the target material of at most $\sim$ 30 fs and $\sim$ 140 fs, which is shorter than the lifetimes of most excited states (1-10 ps).

The emission of gamma rays in flight causes a shift in their detected energy that depends not only on the velocity of the recoils but also on the angle θ between the trajectory of the ions and the direction of motion of the photons, in accordance with Equation 1.8.

$$E_\gamma^{LAB} = \frac{E_\gamma^0}{\gamma(1 - \beta \cos\theta)} \tag{1.8}$$

where $\gamma = (1 - \beta^2)^{-\frac{1}{2}}$ is the Lorentz factor. The phenomenon is called Doppler effect and has to be accounted for in order to recover the energy of the excited levels transitions. To achieve that, accurate measurement of the velocity of the ions and emission angle of the gamma rays are necessary. In experiments with the AGATA-PRISMA setup (see Figure 1.2), the latter is obtained through the reconstruction of the ions trajectory combined with the angular resolution of the array. For the calculation, the emission of the gamma rays is approximated to occur at the center of the target. According to Equation 1.8, the quality of the Doppler correction reflects the resolutions in gamma-ray energy, velocity and reconstruction of the angle of the setup.

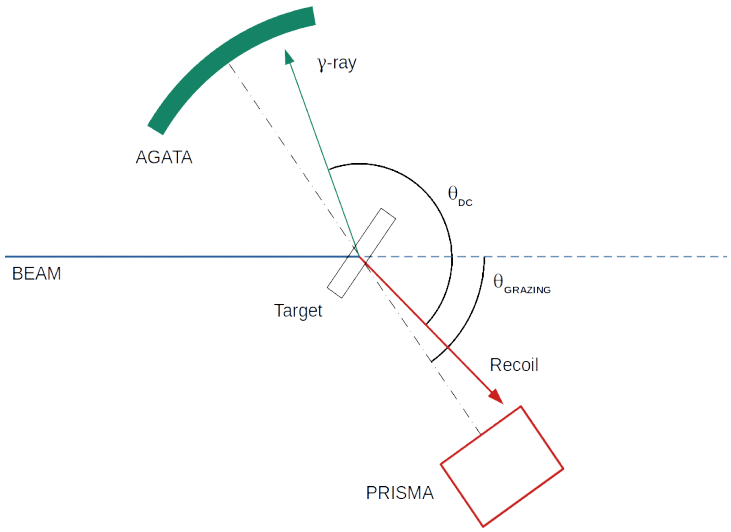

Figure 1.2: Schematic view of the AGATA-PRISMA experimental setup. Both the grazing angle $\theta_{\mathrm{GRAZING}}$ at which the spectrometer is located and the θ_{DC} between the trajectory of the recoils and the direction of motion of the gamma rays are reported in the picture.

In the case of the target-like binary partners, the procedure is more elaborate, as their velocity vector is not measured directly. Indeed, full kinematic reconstruction of the reaction, taking into account also the energy loss inside the target, is necessary. The procedure requires accurate knowledge of the beam energy, target thickness and rotation as well as the velocity vector of the beam-like recoils. In the current in-beam commissioning, the first quantity is monitored and set by the accelerator complex, with a precision on the order of 1/1000. Target parameters are determined mostly before the experiment and the velocity vector is measured in the PRISMA magnetic spectrometer. The energy loss of the beam and beam-like recoils is estimated using the code SRIM [25]. Since it is not possible to locate the interaction position inside the target on an event-by-event basis, all reactions are

assumed to take place at its middle. The momentum of the binary partner is thus calculated through momentum conservation.

$$\vec{p}_{beam} = \vec{p}_{BP} + \vec{p}_{recoil} \tag{1.9}$$

As the mass of the target-like partners is known precisely, thanks to the identification of the reaction channel, the ion velocity and kinetic energy follow as a consequence. The speed of the nuclei at the exit of the target is evaluated after subtracting the energy loss estimated through SRIM calculations. The procedure allows to determine the velocity vector of the target-like recoils and perform the Doppler correction. Moreover, thanks to the energy conservation principle, the Q value of the reaction can be determined as

$$Q_{val} = E_{BP} + E_{recoil} - E_{beam} \tag{1.10}$$

with quantities intended in their value at the moment of the reaction, in the middle of the target. As will be shown in the next Section, coarse knowledge of the TKEL is used to identify, to some degree, high-lying and low-lying excited states transitions. Moreover, the technique is commonly used in experiments on lifetime measurement to remove the feeding from higher-lying states.

1.6 TKEL selection

Total Kinetic Energy Loss (TKEL) discrimination is a powerful tool that allows to infer the excitation energy of the reaction, a quantity that is critical in a number of applications. By only detecting gamma rays it is very difficult to know precisely the entry point of the reaction, since a specific gamma ray can be emitted either following the direct population of the corresponding excited state or from a gamma cascade from higher-lying excited states. Measurements of cross sections or nuclear excited state lifetimes that rely only on gamma detection are affected both by how well the nuclear level scheme is known and by the capability to distinguish all possible feeding transitions. Lifetime measurements in particular can be severely hindered by the presence of long-lived excited states above the state of interest.

In direct reactions, where one or few nucleons are exchanged between projectile and target, usually one can measure the excitation energy of the reaction products with rather good precision. In the past this was extensively done in direct kinematics with light H or He beams impinging on heavy stable targets, detecting the light ejectiles with high-resolution particle spectrometers. The obtained excitation energy resolutions were as good as few keV.

To study nuclei far from the stability with this kind of reactions one has to operate in inverse kinematics (heavy projectile impinging on a light target). In such a case the excitation energy is usually reconstructed by detecting the light ejectile using Si detectors and the obtainable resolutions are of the order of few hundreds of keV. Here the advantage is that the TKEL of the reaction represents the excitation energy of heavy partner alone. An example is reported in Figure 1.3 for the reaction ^{19}O(d,p)^{20}O at 8 AMeV [8] performed at the GANIL facility using the MUGAST-AGATA-VAMOS setup and a 0.3 mg/cm^2 thick CD_2 target. The peaks corresponding to the excited states in the ^{20}O recoils are clearly visible and can be selected through simple gates.

In MNT reactions with heavy ions ($A > 20$) at energies close to the Coulomb barrier, Si detectors do not give enough mass and charge resolutions and the employ of magnetic spectrometers is mandatory to obtain a good identification of the recoils. These setups are best suited for the study of MNT reactions, which typically populate a large number of nuclei, allowing to study multiple channels at the same time. The event-by-event reconstruction of kinematic quantities like velocity, energy and scattering angle allows to compute the TKEL of the reaction but usually the resolutions are not better than few MeV (see Section 1.5 for a full discussion). In addition, the TKEL distribution reflects the excitation of both reaction partners. However, TKEL selection can still be applied to some degree

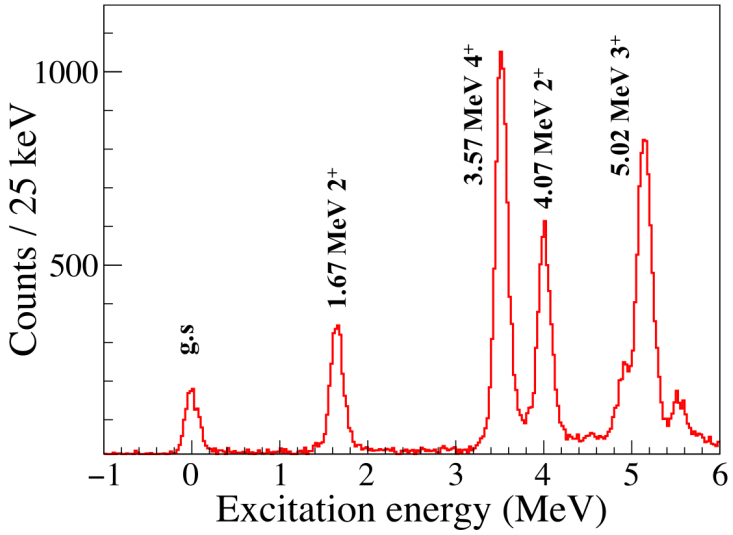

Figure 1.3: Excitation energy spectrum for the ^{19}O(d,p)^{20}O reaction at 8 AMeV using a 0.3 mg/cm^2 thick CD_2 target. Data acquired with the MUGAST-AGATA-VAMOS setup. Taken from reference [8].

to distinguish between transitions originating from high-lying and low-lying states as well as infer information on the reaction mechanism. Lifetime measurements benefit greatly from the use of this method for the removal of feeding from higher-lying states.

The left panels of Figure 1.4 show the effect of the technique in an experiment performed with the PRISMA-CLARA setup, where the reaction ^{90}Zr + ^{208}Pb at 560 MeV was employed along with a 290 μg/cm^2 thick target [14]. The procedure allowed to further prove the presence of neutron evaporation in the target-like fragments for high values of TKEL and to remove its contribution, by gating on the low values, in order to study the desired nucleus. The right panel of Figure 1.4, on the other hand, shows the results of the implementation of the same technique in the context of lifetime measurements. The experiment employed the Recoil Distance Doppler Shift method for the study of the reaction ^{48}Ca + ^{208}Pb at 310 MeV using the PRISMA-CLARA setup. The target had a thickness of 1.0 mg/cm^2 and a backing of 1.0 mg/cm^2 of Ta. TKEL selection was employed to evaluate the contribution of feeding from higher-lying excited states.

One of the objectives of the in-beam commissioning of the AGATA-PRISMA setup has been to test the possibilities offered by the TKEL selection in the current experiment. A full discussion of the results is reported in Section 4.2.5 of this work.

1.7 Outline of the work

As discussed in Section 1.2, the focus of this thesis is the evaluation of the capabilities of the AGATA-PRISMA combined setup, with specific regard to the performance of the magnetic spectrometer, the quality of the final Doppler correction and the possibilities offered by the kinematic reconstruction of the reaction. In this Section we will briefly outline the structure of this work, which is organized as follows:

- In Chapter 2, the configuration of the AGATA-PRISMA setup in its first in-beam commissioning experiment will be presented. Since the work will focus more on the magnetic spectrometer, more time is devoted to its description. The reasons for and advantages gained through the coupling of the two apparatuses are discussed in Section 1.1.
- Chapter 3 will present the different phases of the commissioning experiment and describe separately the analysis and data processing of the two apparatuses. Again, more space will be

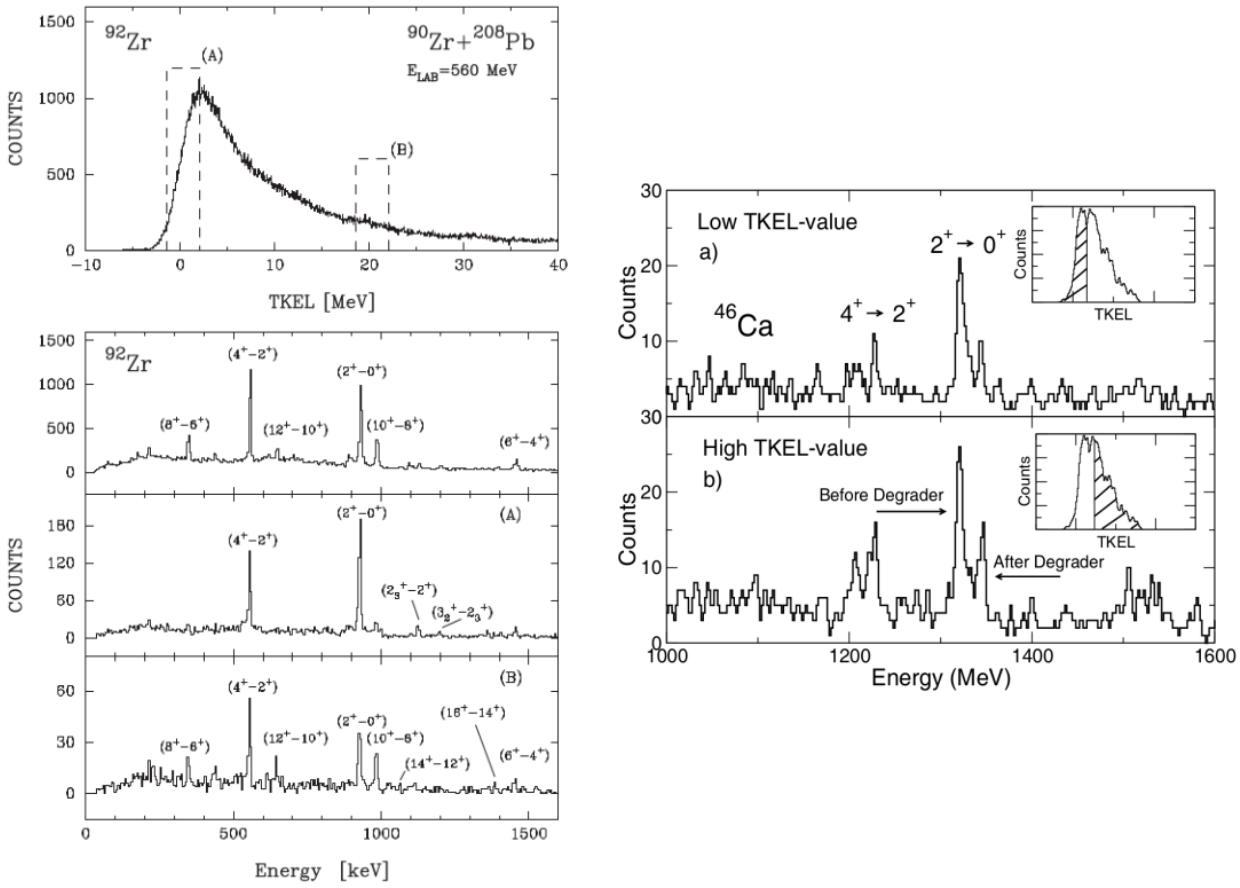

Figure 1.4: TKEL selection with the PRISMA-CLARA setup in the context of the reactions ^{90}Zr + ^{208}Pb at 560 MeV (left, taken from [14]) and ^{48}Ca + ^{208}Pb at 310 MeV (right, taken from [26]). In the left panels, the technique was used to evaluate the contribution of neutron evaporation of the target-like fragments. In the right panel, instead, the method was employed for lifetime measurement. See text for a full discussion.

devoted to the detailed discussion of the PRISMA data processing.

- In Chapter 4 the merging procedure for the two streams of data will be described. The performance of the setup in its first in-beam commissioning experiment will be discussed, in terms of overall capabilities of the PRISMA spectrometer, quality of the Doppler correction and Total Kinetic Energy Loss (TKEL) discrimination of the gamma-ray transitions.

Chapter 2

Experimental Setup

The experiment described in this thesis was performed at the INFN Legnaro National Laboratories (LNL) in Italy in April 2022. The aim was the evaluation of the performance of the newly installed experimental setup involving the coupling of the PRISMA large acceptance magnetic spectrometer and the Advanced GAmma Tracking Array (AGATA). Multi-nucleon transfer reactions and excitation below the Coulomb barrier, with different combinations of beam and target, were selected for the commissioning of the apparatuses. This Chapter will describe the setup in its main components.

2.1 The PRISMA magnetic spectrometer

PRISMA [10, 27, 28] is a large acceptance magnetic spectrometer designed for the identification of medium mass reaction products from heavy ion collisions ($20 < A < 150$) with energy in the range of 3-10 MeV/u. Similar high performance, low energy magnetic spectrometers of this kind are VAMOS at GANIL [18, 29] and MAGNEX at INFN - LNS [16]. The main characteristics of the device are shown in Table 2.1.

Resolution		
Z resolution	ΔZ/Z	1/60
A resolution	ΔA/A	1/300
Energy resolution	ΔE/E	1/1000
Acceptance		
Energy acceptance	$\pm$20	%
Momentum acceptance	$\pm$10	%
Solid Angle	80	msr
Azimuthal acceptance	$\pm$ 6	deg
Polar acceptance	$\pm$ 11	deg

Table 2.1: Main characteristics of the PRISMA magnetic spectrometer. Taken from reference [10].

These are achieved thanks to the reconstructions of the trajectory of the ions inside the apparatus. Figure 2.1 presents a schematic view of the spectrometer:

- A Micro-Channel Plate (MCP) detector serves as entrance detector for the apparatus, measuring the position of the ions in their x and y components as well as providing a first time signal for Time of Flight (ToF) measurement.
- A single quadrupole magnet focuses the reaction products in the vertical plane (y axis), while defocusing on the horizontal one (x axis).

- A dipole magnet curves the ions trajectory according to their magnetic rigidity, thus allowing to perform their identification at a later stage.
- A large Multi Wire Parallel Plate Avalanche Counter (MWPPAC) is placed at the focal plane of the spectrometer and is used to measure the position of the reaction products along the x and y axis as well as provide the second time signal for ToF measurement.
- An array of Ionization Chambers (IC) is positioned after the MWPPAC and allows to measure energy loss and total energy of the ions that reach the end of the spectrometer.

The spectrometer can rotate around the target position in the angular range going from -30° to +130°, with respect to the beam axis. We will now proceed to describe in detail each of the elements that compose the apparatus.

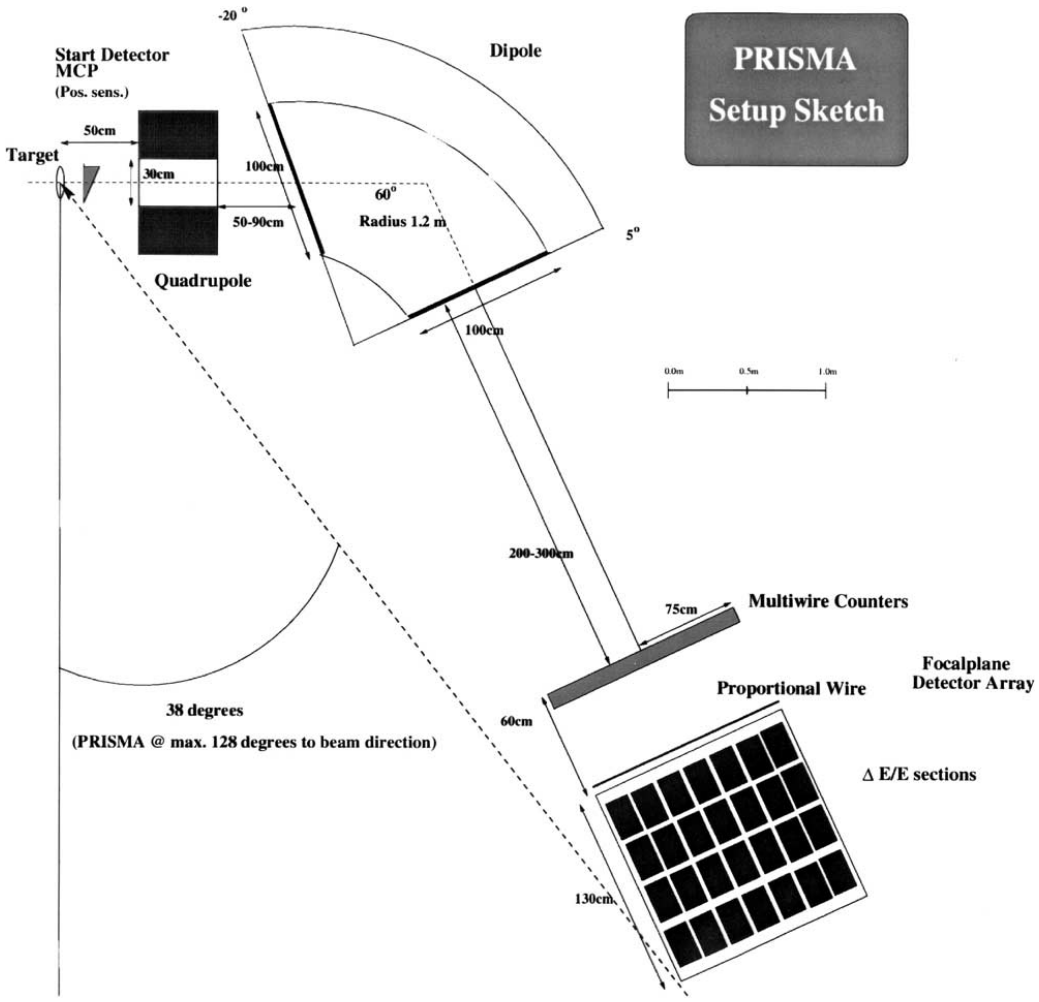

Figure 2.1: Schematic top view of the PRISMA magnetic spectrometer. Sketch from reference [10].

2.1.1 The Micro-Channel Plate detector

The MCP entrance detector [27] is mounted 250 mm from the target in Chevron configuration. Figure 2.2 presents a schematic view of the detector as well as a picture before the assembly. A thin carbon foil is placed across the ions path at 250 mm from the target, rotated by 45°. The reaction products passing trough it produce secondary electrons, which are then accelerated by an electric field towards a position sensitive anode. During this migration they are subject to a magnetic field directed from the carbon foil to the anode. This results in the spiralization of the electron trajectories, which limits transverse motion, thus increasing position resolution. Once the anode is reached, the MCP behaves as a photo-multiplier tube so that the number of electrons is amplified by a factor $\sim 10^5 - 10^6$. Finally, making use of windings of gold plated tungsten wires as delay lines, the resulting signals carry

information about time and position of the ions going through the carbon foil.

The intrinsic time resolution (FWHM) of the detector is around $300 - 400$ ps, to be quadratically summed with the time resolution of the MWPPAC to obtain total ToF resolution. On the other hand, the position resolution of the MCP detector is approximately ~ 1 mm in both x and y directions. At 250 mm of distance from the target this corresponds to an angular resolution of $\sim 0.2°$ in the determination of the recoils initial direction, assuming the beam to be focused and centered on the target. Finally, the intrinsic efficiency of the MCP detector for the detection of heavy ions is typically close to 100 %.

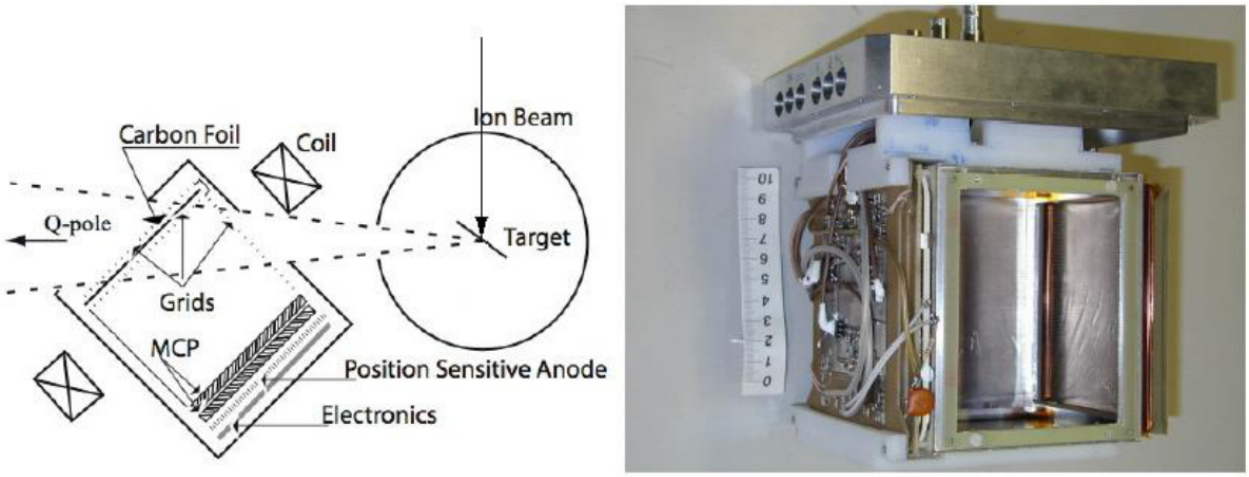

Figure 2.2: Schematic view of the MCP entrance detector (left). Picture of the MCP detector (right). Pictures taken from reference [27].

2.1.2 The optical elements

The purpose of the PRISMA optical system is to first focus the reaction products onto the focal plane of the spectrometer and later bend their trajectories according to their magnetic rigidity.

A quadrupole singlet is placed downstream of the MCP detector at 500 mm from the target. Its magnetic field focuses the incoming ions along the vertical axis and disperses them along the other, thus increasing the acceptance of PRISMA in ϕ (azimuthal angle with respect to the beam axis) while decreasing the one in θ (polar angle with respect to beam axis). The magnet has an entrance window diameter of 320 mm and a length of 420 mm, however its fringing field extends beyond this region. Therefore, in the analysis, an effective length had to be determined and substituted to the geometrical one (see Section 3.2.5).

A large dipole magnet is placed 600 mm downstream of the quadrupole exit window, bending the trajectories of the ions according to their magnetic rigidity. The maximum magnetic rigidity is 1.2 Tm, considering a bending angle of 60°, corresponding to a curvature radius of 1.2 m, and a maximum magnetic field of 1 T.

2.1.3 The Multi-Wire Parallel Plate Avalanche Counter

A large area MWPPAC detector [28] is located at the focal plane of the PRISMA spectrometer, 3.28 m from the dipole exit window. Its purpose, similarly to the entrance detector, is to measure position and time of the ions passing through it. A picture of the MWPPAC along with a 3D rendering can be seen in Figure 2.3. The sensitive area of the detector consists of a gas chamber with dimensions 1000 x 130 x 8 mm^3 filled with isobutane (C_4H_{10}) at 7-8 mbar of pressure. Two large mylar windows, 1.5 μm thick, separate gas from vacuum. These are supported by 100 μm thick vertical stainless steel wires placed every 3.5 mm.

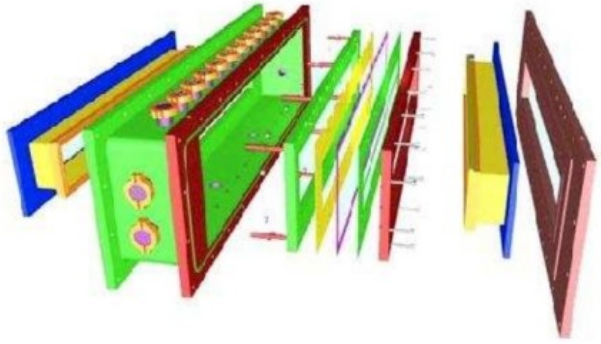

Figure 2.3: The MWPPAC detector during its assembling on the PRISMA spectrometer (left). 3D rendering of the MWPPAC detector (right). Pictures taken from reference [28].

Inside the chamber, the MWPPAC has a three electrode structure: the central cathode, biased at 500-600 V, consists of a plane of gold plated tungsten wires 20 μm thick stretching vertically across the detector with a step of 0.33 mm. The X anode, 1 mm behind the cathode, has a similar structure, though the wires are spaced 1 mm apart from each other. These two are both divided into 10 separate identical sections, each with an active area of 100 x 130 mm^2. Finally, the Y anode is common to all sections and consists of a plane of 130 similar wires extending horizontally 1000 mm long with a step of 1 mm. As the Y direction is not critical in the trajectory reconstruction, these wires are connected in groups of two, in order to decrease signal attenuation.

When the reaction products pass through the detector, they each leave a trail of ionized gas. Under the influence of the electric field, the electrons migrate toward the two anodes and the positive ions toward the cathode. Due to the geometry of the wires, the electric field is much higher in their vicinity. If the field is high enough, the electrons and the ions gain sufficient kinetic energy to ionize other gas molecules (secondary ionization), which in turn can be accelerated and produce further ionization. The process repeats, in a phenomenon know as *Townsend avalanche* [30], resulting in a large amount of collected charge, accompanied by the loss of information on the amount of initial ionization and thus on the energy loss. Although this fact does not pose an issue for the task at hand, as measuring energy loss was never one of the objectives of the MWPPAC, it is worth mentioning, as this will be relevant in the case of the ionization chamber.

Finally, the collected charge induces a signal suitable for the read-out electronics. The X and Y anodes employ the concept of delay lines to gain information about the position of the ions, while, in the case of the cathode, the wires of each section are short circuited in order to obtain a position independent fast timing signal, used for ToF measurement. The position resolution of the detector has been measured to be $\sim$ 1 mm in the X direction and $\sim$ 2 mm in the Y direction. The time resolution is similar to the entrance detector at around $300 - 400$ ps, while the intrinsic efficiency of the MWPPAC is typically close to 100 % in standard working conditions with heavy ions.

2.1.4 The Ionization Chambers

A segmented transverse-field Ionization Chamber (IC) [28], shown in Figure 2.4, is located at the end of the spectrometer, 60 cm downstream of the MWPPAC detector. The IC measures the total energy and partial energy loss of the ions in order to perform Z identification through the $\Delta E - E$ technique. Its sensitive volume has dimensions 1100 x 200 x 1200 mm^3 and can be filled with either high-purity methane (CH_4) or carbon tetrafluoride (CF_4), at pressures ranging from 15 mbar to 100 mbar, depending on the penetrative capabilities of the ions. These gases have particularly high electron and ion drift velocities, which allow to reach relatively high counting rates ($\sim$ 5 kHz) in spite of the large gas volume. To separate the gas from the vacuum, a large mylar window with a 1.5 μm thickness

is placed at the entrance and supported by 1000 stainless steel vertical wires of 100 μm in diameter spaced 1 mm apart. The electrodes of the IC are segmented into 40 central pads (width 10 cm, length 30 cm) and 8 side pads (width 5 cm, length 30 cm). The side pads ensure electric field linearization and are used as veto for the IC in the data processing.

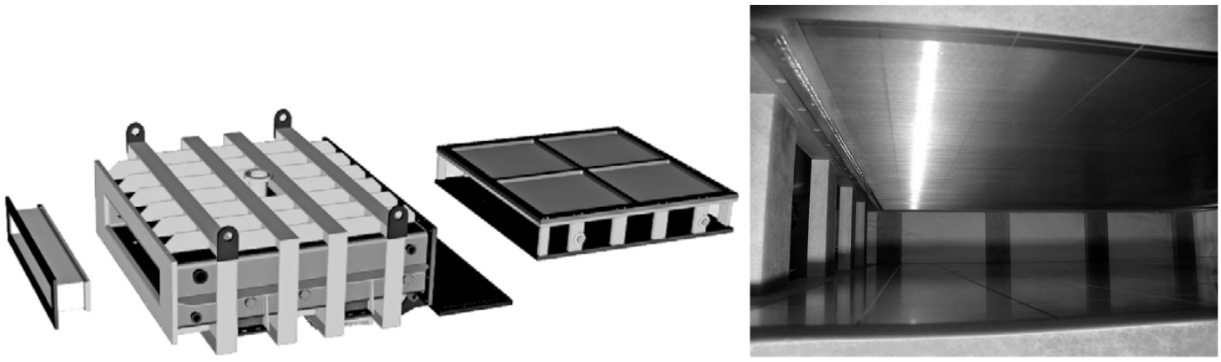

Figure 2.4: Schematic layout of the PRISMA ionization chambers (left). Inner view of the ionization chamber (right). Taken from reference [28].

As the reaction products traverse the mylar window and enter the IC, they gradually lose energy inside the gas until they are eventually stopped, in accordance with *Bethe equation* [31]:

$$-\frac{dE}{dx} = \left(\frac{1}{4\pi\epsilon_0}\right)^2 \frac{4\pi e^2}{m_e}\frac{(ze)^2}{v^2} n_e Z \left[ln\left(\frac{2m_e v^2}{W}\right) - ln(1-\beta^2) - \beta^2\right] \tag{2.1}$$

where $-\frac{dE}{dx}$ is the energy loss per unit length, also called *stopping power*, e and m_e are the charge and rest mass of the electron, ze and $v = \beta c$ are the atomic charge and velocity of the ion going through the chamber, n_e and Z are the electron density and atomic number of the absorber and W is the average energy needed to produce an electron-ion pair in the gas. The process leaves a trail of ionized molecules inside the chamber. The number of electron-ion pairs that are produced is proportional to the energy deposited. Under the influence of the electric field, the electrons migrate toward the anode and the ions toward the cathode. A Frisch grid is placed 25 mm in front each of the anode (see Figure 2.4, right panel), ensuring that the amplitude of the signal does not depend on the distance of the detected ion from the anode.

The charge collected in each pad represents a measurement of the energy lost by the reaction products in the corresponding region of the detector. This quantity is proportional to the nuclear charge ze of the recoils, in accordance with Eq. 2.1, and can therefore be used to perform Z identification through the $\Delta E - E$ method. The technique requires the selection of a first detection layer used to slow down the ions and a second layer where the particles are stopped. By plotting the energy loss detected in the first layer versus the total energy of the nuclei, a number of repeating structures appear, each corresponding to ions with a certain atomic number, as shown in Figure 2.5. In the case of PRISMA, the first two rows of pads are typically used as ΔE layer, while the whole IC is used to measure the total energy of the incoming particles. This allows to perform Z identification with typical resolutions of $\Delta Z/Z \sim 1/60$.

Recently both the front-end and back-end electronics of the IC have been refurbished. In the current configuration, the 40+8 signals of the IC are sent directly to 3 Mesytec MPR-16 unipolar preamplifiers with a selectable 60 - 300 MeV range through 50-cm long LEMO – DB-25 cables. Additional LEMO cables are transporting the preamplifier signals to 3 Mesytec MSCF-16 shaping amplifiers. Energy outputs are then sent to a V755 ADC, while part of the CFDs signals are sent to a V775 TDC for the measurement of the drift time.

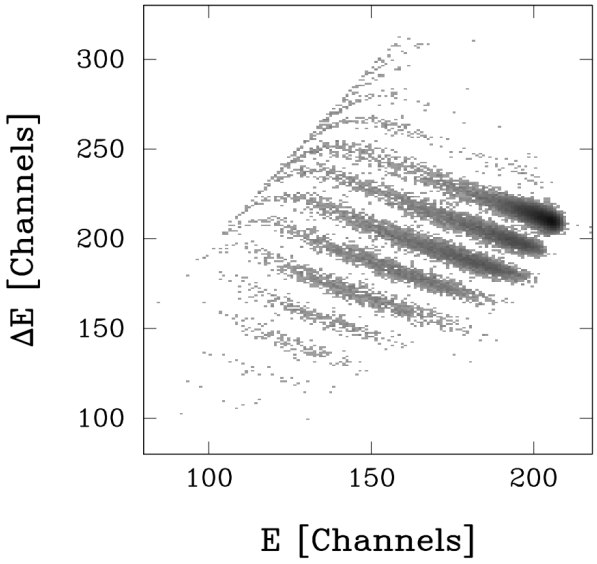

Figure 2.5: Example of a two-dimensional $\Delta E - E$ spectrum for the reaction ^{40}Ca + ^{208}Pb at 235 MeV. Taken from reference [24].

2.2 The AGATA array

The Advanced GAmma Tracking Array (AGATA) [4, 6] is a gamma-ray spectrometer composed of segmented high-purity germanium (HPGe) detectors that currently represents the state of the art of gamma-ray detection, along with the similar GRETA array [3] in the United States. The apparatus has a modular structure designed to cover almost completely the 4π solid angle (see Figure 2.6) and is based on the novel concepts of gamma-ray Tracking and Pulse Shape Analysis (PSA). The basic unit of the array is the Agata Triple Cluster (ATC), shown in Figure 2.6, which includes three asymmetric, hexagonal shaped, germanium crystals, along with the supporting structure, a number of preamplifiers and a cryostat. The full 4π design requires 60 ATCs, for a total of 180 germanium crystals covering 82% of the full sphere.

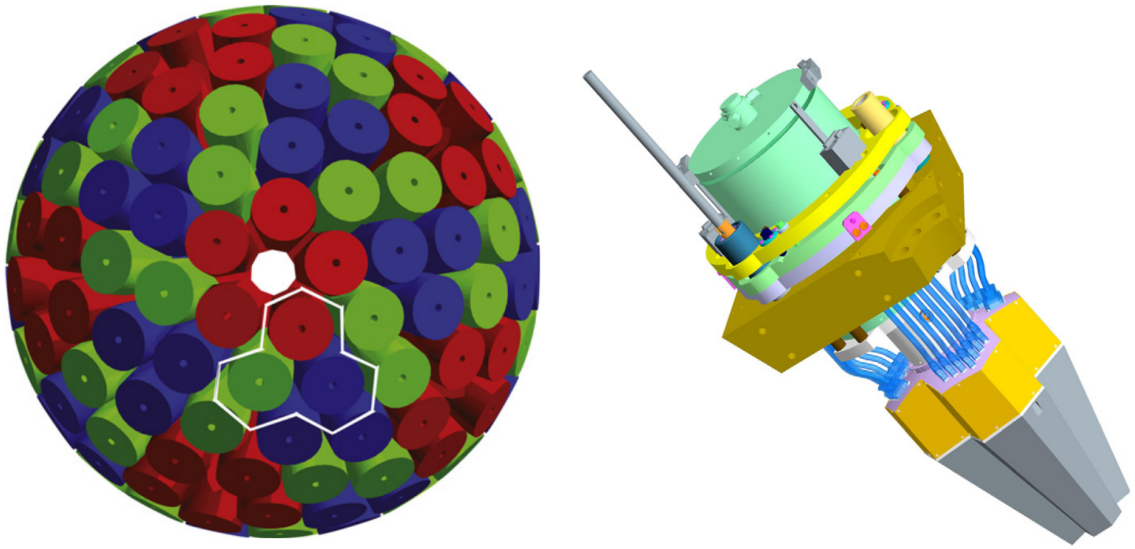

Figure 2.6: Schematic view of the full 4π configuration of the AGATA array (left). 3D rendering of an Agata Triple Cluster (right). Taken from reference [32].

The project is the result of a European collaboration and for the last decade has been gradually expanding while travelling through Europe at stable and radioactive beam facilities, namely the INFN

Legnaro National Laboratories (2009-2011) in Italy [6], GSI (2012-2014) in Germany [7] and GANIL (2015-2021) in France [8]. More recently, in 2021, the apparatus has been dismantled from GANIL and, in 2022, rebuilt at LNL (Legnaro National Laboratories). Here AGATA has been coupled to the PRISMA magnetic spectrometer and further expansion of the array is under way to reach its 1π configuration for the first time. A picture of the current setup along with a schematic view of the foreseen 1π configuration can be seen in Figure 2.7. The AGATA array was placed in opposition to PRISMA and is able to rotate in conjunction to the magnetic spectrometer. This addition restricts the movement of PRISMA to the angular range going from $+20°$ to $+82°$.

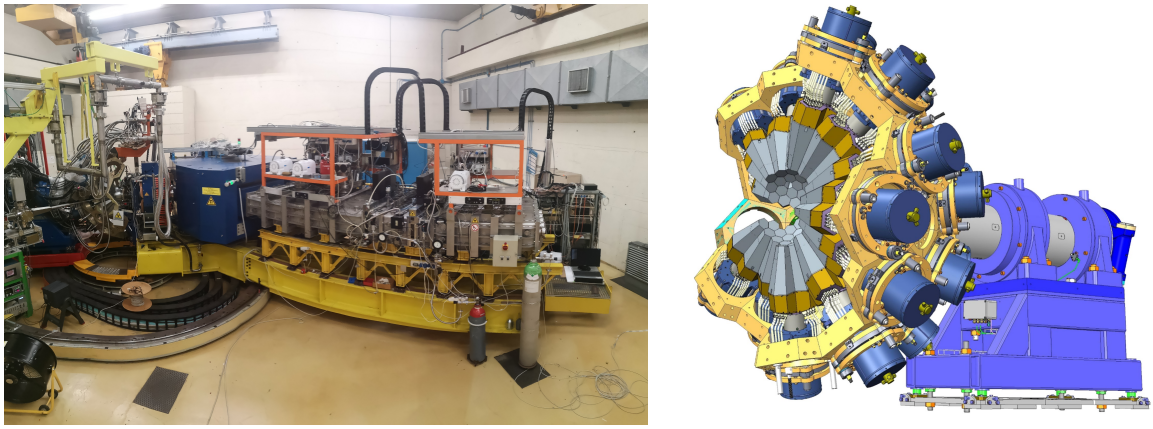

Figure 2.7: The AGATA-PRISMA setup (left). Schematic view of a single segmented HPGe crystal (right).

The right panel of Figure 2.8 shows how the HPGe crystals are segmented. They are n-type in nature and present a coaxial configuration. A common central contact, denominated *core*, is shared by all 36 segments, allowing to collect all the negative charges produced by the ionization process. The positive charges are instead collected locally in each segment through individual connections. Each segment is equipped with a two stage preamplifier, of which the first portion located in the nitrogen cooled region of the ATC. The core, on the other hand, has been provided with two of such preamplifiers with different gains, for a total of 38 signals per germanium crystal.

When a gamma ray interacts with the detector the resulting ionization induces mirror signals in the neighboring segments. Using PSA algorithms it is possible to reconstruct the position of the interaction with a precision of ~ 5 mm of Full Width at Half Maximum (FWHM) [4]. Each hit therefore carries information on interaction position, time and energy deposition. The tracking algorithm is then able to correlate among each other the hits measured in a single event, taking into account the three gamma interaction processes, photoelectric absorption, Compton scattering and pair production, and recognise which hits are related to the same initial gamma ray. The initial interaction position is then determined along with the total energy deposited by the gamma ray in the apparatus. The process is able to greatly increase the peak to total ratio of the gamma spectra, as Compton measurements are effectively suppressed. In particular, the expected performance of the conceptual 4π design reach a photopeak efficiency of 43% and a peak-to-total ratio of 59% for 1-MeV photons produced in events of multiplicity one, along with an intrinsic energy resolution of about 3/1000 and an angular resolution of $\sim 1°$.

For the first commissioning experiment of the current campaign at Legnaro National Laboratories the AGATA array consisted of 9 ATCs arranged as shown in the left panel of Figure 2.8.

Figure 2.8: The AGATA array during its first commissioning at Legnaro National Laboratories in April 2022 (left). Schematic view of a single segmented HPGe crystal of the AGATA array (right). Right panel is taken from reference [4].

Chapter 3

Data Processing

This Chapter will first present the in-beam commissioning experiment of the AGATA-PRISMA setup and then discuss the data processing of the two apparatuses.

3.1 The Commissioning Experiment

The experiment presented in this work was performed at the Legnaro National Laboratories [9] of INFN in April 2022. Its aim was the commissioning of the newly installed AGATA-PRISMA setup, which has been described in detail in Chapter 2. During most of the experiment, the global trigger of the read-out data acquisition system was the OR of all cathode signals coming from the MWPPAC of the PRISMA spectrometer. The commissioning lasted 7 days and was composed of a number of phases.

In a first phase, a beam of ^{58}Ni was accelerated by the TANDEM accelerator to an energy of 225 MeV (3.9 MeV/u) and delivered perpendicularly onto a target of ^{197}Au with a thickness of 0.2 mg/cm^2, resulting in a mid-target collision energy about 20% below the Coulomb barrier. In these conditions, the two nuclei interact mainly through elastic or inelastic scattering mediated by the Coulomb field and transfer cross sections are very low. As a consequence, the recoils detected in PRISMA were almost exclusively ^{58}Ni nuclei with a very narrow energy distribution, due to the low thickness of the target, which resulted in nearly ideal conditions for the setting of the electronics of the spectrometer, in terms of thresholds, shaping times, trigger for the acquisition and so on. Gamma-ray production, on the other hand, was relatively low and not optimal to test the capabilities of the AGATA array. Indeed, the purpose of this phase was mainly to determine the initial settings of the PRISMA spectrometer, test the newly installed electronics and verify the correct operation of the pumping and vacuum systems.

Once stable experimental conditions were achieved, the beam was swapped to ^{32}S at 160 MeV (5 MeV/u). In this next phase, two targets of ^{124}Sn with thicknesses of 0.5 and 2.5 mg/cm^2 were employed. The analysis presented in this work focuses on the runs with the thinner of the two. The target was rotated by 35° with respect to the beam direction, resulting in a mid-target collision energy about 30% above the Coulomb barrier. During the experiment the PRISMA magnetic spectrometer was placed at the grazing angle of 55°, in order to maximize the probability to detect the products of transfer reactions. Figure 3.1 shows the most intense reaction channels, as predicted using the GRAZING code [23]. Proton stripping and neutron pick-up channels dominate the transfer flux, indicating that the reaction mainly populates nuclei located south-east of the beam ion ^{32}S in the nuclear chart. As explained in Chapter 1, this type of reactions populates a variety of moderately exotic nuclear species in a multitude of excited states, leading to a large production of gamma rays at different energies. Such conditions are optimal to fully test the performances of the AGATA-PRISMA setup.

After the beam was swapped to ^{32}S, the electronics settings were readjusted, as well as the gas pressures and working voltages of the MCP, MWPPAC and IC detector elements of the magnetic

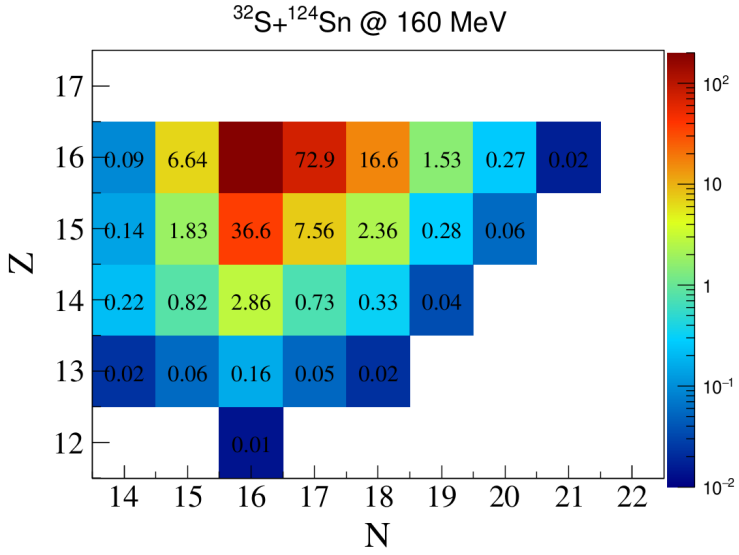

Figure 3.1: Predictions obtained with the GRAZING code in regards to the total transfer cross sections for the ^{32}S + ^{124}Sn reaction at 160 MeV. Values are expressed in units of mb. Taken from reference [12].

spectrometer. In addition, the intensities of the fields inside the two magnets were also modified, so that the trajectories of the recoils belonging to the more statistically significant atomic charge states of the elastically scattered ^{32}S would intercept the central region of the MWPPAC. Furthermore, this choice ensures that no binary partner nuclei would reach the focal plane of the spectrometer and trigger an event as, due to their lower velocity, their trajectories were always bent towards the inner wall of the PRISMA vacuum chamber.

In this thesis, the data corresponding to the runs with the ^{32}S beam at 160 MeV impinging on a ^{124}Sn target 0.5 mg/cm^2 thick were analyzed to evaluate the performance of the setup. These correspond to $\sim$ 21 hours of acquisition where the PRISMA MWPPAC served as global trigger and the beam intensity was averaging approximately 3.5 pnA plus $\sim$ 14 hours where both apparatuses acquired in triggerless mode and the beam intensity was lowered to about 1.0 pnA.

3.2 PRISMA data processing

The final purpose of PRISMA is to identify the incoming ions in velocity $\vec{\beta}$, atomic number Z and mass number A, by combining the information obtained from all of its components. To this aim, the data processing goes through different steps:

- First is the setting of the thresholds and the calibration of the various elements of the spectrometer. The latter is achieved using a number of methods to obtain the reference values that concern the MCP and MWPPAC, while for the IC a simple gain matching between the different pads is carried out.
- The event by event Z identification of the recoils can be performed directly after the calibration of the IC using the $\Delta E - E$ technique, as described in Section 2.1.4.
- Next is the calibration and thresholds setting of the Time-of-Flight (ToF) signals, followed by the alignment of the various sections of the MWPPAC.
- The ions trajectory reconstruction is then performed using the position information coming from the MCP and MWPPAC as well as the knowledge of the magnetic fields of the two optical elements. This allows to obtain the magnetic rigidity $B\rho$ and path length L of the ions, which together with the ToF yields their velocity β and A/q ratio.

- The atomic charge state q is obtained through 2D polygonal gates in the E (energy, measured in the IC) versus $\rho\beta$ plot.
- Finally, the mass spectrum is calculated by multiplying the Z and q gated A/q distributions by effective non-integer charge values.

We will now proceed to discuss each of these phases in detail, starting from the raw data acquired by the PRISMA 12-bit resolution ADC's and the TDC's.

3.2.1 MCP calibration

Details on the structure and operating principles of the MCP entrance detector have been reported in Section 2.1.1. As previously mentioned, the main purpose of the device is to record the time and position of the recoils entering the spectrometer on an event-by-event basis. Such measurement is critical in order to accurately determine the velocity vector of the incoming ions. Figure 3.2 shows the comparison between the raw and the calibrated two-dimensional position distributions of the ions detected by the MCP. A 2D gate, highlighted in green in the plot, is applied to the raw data in order to avoid spurious events caused by inefficiencies and false triggers, effectively removing any overflows and underflows of the electronics. In addition, during the experiment, a metal cross was placed in front of the detector, creating a shadow in both spectra by stopping part of the incoming ions. The center of the cross and the marks on each arm, emphasized in red in Figure 3.2, serve as reference points for the calibration of the MCP. Furthermore, both spectra present a region of low statistics, located to the right of the cross center in one case and to its left in the other, clearly indicating the presence of a loss of efficiency, discussed in more detail in Section 4.1.1 of this work.

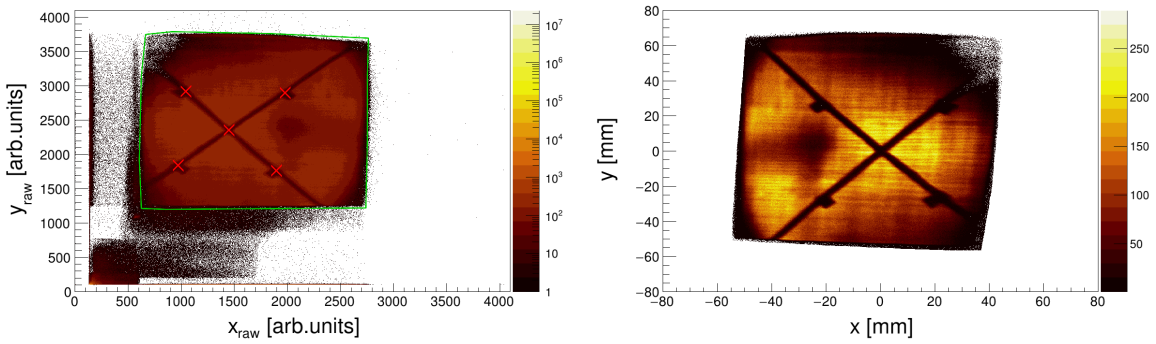

Figure 3.2: Comparison between the raw (left) and calibrated (right) MCP spectra. In the left panel, a 2D gate, highlighted in green, is used to discriminate between meaningful events and random noise, while the red crosses indicate the reference points used for the calibration.

Position	x (mm)	y (mm)
center	0	0
top left	-21.5	26.5
top right	21.5	26.5
bottom left	-21.5	-26.5
bottom right	21.5	-26.5

Table 3.1: Positions of the reference points corresponding to the center and the markings on each arm of the cross placed in front of the MCP detector.

To convert from the initial raw data to the calibrated picture, the strategy involves a multi-step, multi-parametric transformation, which allows to effectively take into account possible deformations due to cross talk effects between the two x and y signals. The procedure is summarized in the equations reported below. First the raw coordinates are "stretched" through the multiplication by a 2D matrix of coefficients with unitary diagonal elements.

$$\begin{pmatrix} x' \\ y' \end{pmatrix} = \begin{pmatrix} x_0 & x_1 \\ y_0 & y_1 \end{pmatrix} \begin{pmatrix} x_{raw} \\ y_{raw} \end{pmatrix} \tag{3.1}$$

Next, quadratic and linear calibrations are applied to the x' and y' coordinates respectively.

$$\begin{cases} x'' = a + bx' + c\,(x')^2 \\ y'' = d + ey' \end{cases} \tag{3.2}$$

Finally, a rotation of angle θ is implemented.

$$\begin{pmatrix} x_f \\ y_f \end{pmatrix} = \begin{pmatrix} \cos\theta & \sin\theta \\ -\sin\theta & \cos\theta \end{pmatrix} \begin{pmatrix} x'' \\ y'' \end{pmatrix} \tag{3.3}$$

The values of the parameters were obtained by minimizing the figure of merit defined in Equation 3.4, corresponding to the sum of the squared distances between the reference points real positions (x_{ref}, y_{ref}), reported in Table 3.1, and their calibrated counterpart.

$$S = \sum_{i=1}^{N} \left[(x_f - x_{ref})^2 + (y_f - y_{ref})^2 \right] \tag{3.4}$$

3.2.2 MWPPAC calibration

The main purpose of the MWPPAC detector (see Section 2.1.3 for a full description), similarly to the entrance detector, is to record the time and position of the reaction products reaching the focal plane of the spectrometer. In addition, during the experiments, the OR of all cathode signals typically serves as trigger for the PRISMA read-out and acquisition system.

For each event, the detector acquires a total of 32 variables, corresponding to the x_l (left), x_r (right) and *cath* (cathode) signals from each of the 10 sections of the MWPPAC, plus the two common y_u (up) and y_d (down). Figure 3.3 shows some typical raw spectra. The central peak in the x_l distribution serves as a reference during the calibration and is caused by the intentional shortening of the two central wires of each section. Furthermore, the cathode variable is the difference in time between the actual cathode signal of the corresponding section and the delayed OR of all cathodes. Such time difference is mostly constant, oscillating only due to electronic noise, and is mainly used to reject non-physical counts. However, since the overwhelming majority of the events recorded in PRISMA have reaction products multiplicity of one, only one section fires at a given time. As a result, approximately 90% of the counts of the x_r, x_l and *cath* spectra fall necessarily into overflow/underflow. Upper and lower thresholds, highlighted in red in Figure 3.3, are therefore applied to each distribution.

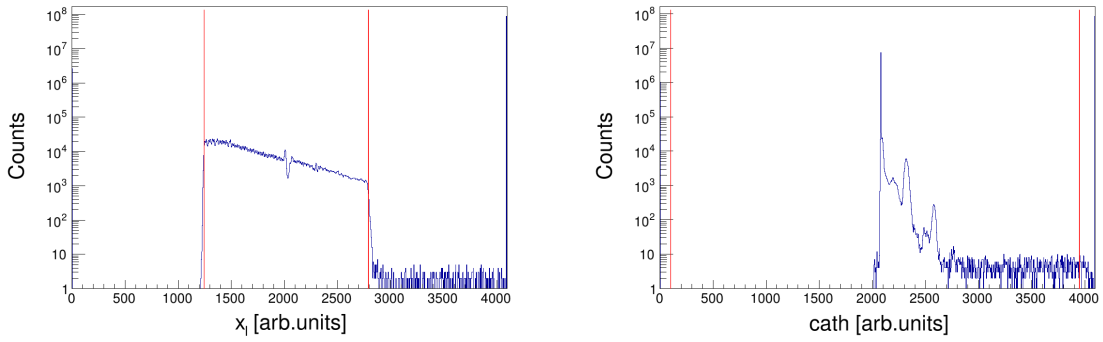

Figure 3.3: Raw spectra of the x_l (left) and *cath* (right) signals of section 5 of the MWPPAC. In each panel the thresholds used for the validation of the measurement have been highlighted in red.

The position x_{fp} of the detected ions on the focal plane is obtained from the x_r and x_l signals:

$$x_{fp} = x_r - x_l \tag{3.5}$$

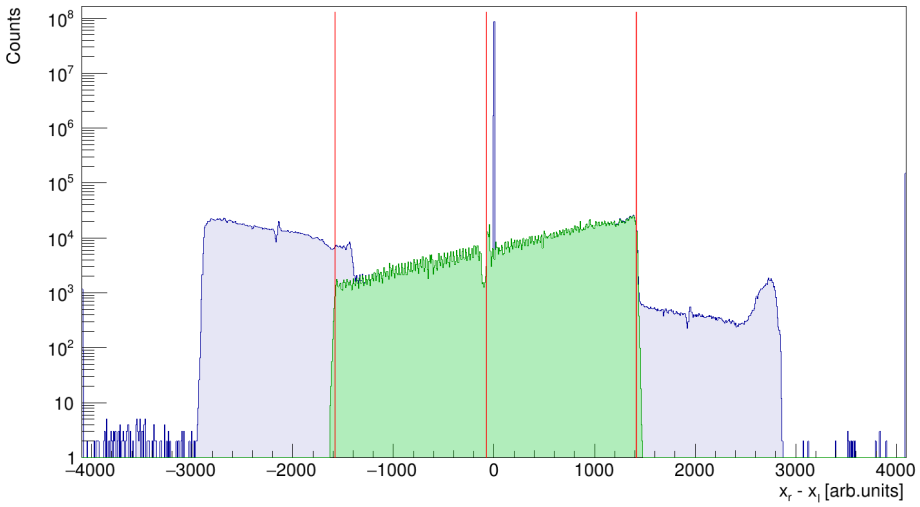

Figure 3.4: $x_r - x_l$ distribution for section 5 of the MWPPAC. The blue histogram indicates the raw distribution, while the green region represent events where neither of the two variables x_r or x_l goes into overflow/underflow. The reference values corresponding to start, center and end positions of the MWPPAC section, used for the x_{fp} calibration, are highlighted in red.

As an example, Figure 3.4 shows the resulting spectrum for a single section of the MWPPAC. By selecting only those events where neither of the two variables x_r or x_l falls into overflow/underflow, the green distribution is obtained. Furthermore, here the three abscissa highlighted in red correspond to the MWPPAC section start, center and end and are used to perform a linear calibration of the focal plane position. The rest of the spectrum, on the other hand, represents events where one of the two signals is lost through attenuation, forming structures that resemble scaled repetitions of the green distribution. This effect is most likely due to the low atomic number of the nuclei at play ($Z \sim 16$), which results in a relatively modest amount of ionization in the gas, in accordance with Equation 2.1, leading to a limited amount of collected charge and therefore a weaker signal. In such cases, a calibration that takes into account only one of the two $x_r - cath$ and $cath - x_l$ variables can be employed to retrieve the information on the focal plane position and increase the efficiency. The resulting final x_{fp} spectrum is displayed in Figure 3.5.

An unusual behaviour is clearly recognizable in some of the sections. In section 0, an unexpected increase in statistics is present between 80 and 100 mm. A more detailed investigation reveals that the corresponding cathode signal is particularly noisy, leading to a sub-optimal x_{fp} reconstruction when one of the two x_r, x_l signals is lost and causing the observed behaviour. When scaled to a higher number of counts, section 1 does not show any abnormalities, indicating that its low statistics is due only to a loss of efficiency. This can be caused either by a high CFD threshold or by the fact that the pad is not working at its best operational conditions. The HV is in fact distributed to the 10 pads of the MWPPAC detectors in groups of 5 by two SILENA 7716 HV modules and it may occur that the set HV value is not optimal for a particular section. Being the charge multiplication exponential in character, an under-bias of 10 V over 500 V may result in large inefficiencies. Lastly, regarding section 9, all cathode signals appear to be in overflow/underflow, resulting in the rejection of all the corresponding events. This may be caused by mechanical reasons, such as a broken contact or a malfunctioning element of the electronics. A detailed discussion on the partial efficiencies of the detector is reported in Section 4.1.4 of this work.

The focal plane distribution shows two wide peak-like structures in the central region of the detector.

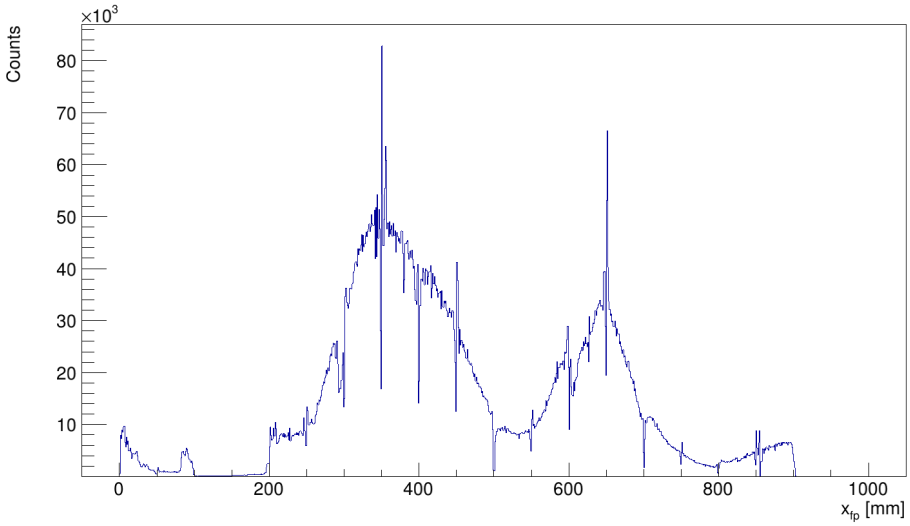

Figure 3.5: Experimental x_{fp} (focal plane position) distribution.

Indeed, due to the limited thickness of the target, the energy spread of the recoils entering PRISMA is relatively narrow, and so is, as a consequence, the $B\rho$ distribution (see 3.11). This leads to a clear separation of the atomic charge states at the focal plane of the spectrometer. The two main structures visible in Figure 3.5 correspond to the 14^+ and 15^+ charge states of recoils.

3.2.3 IC calibration and Z identification

The details on the design of the transverse-field Ionization Chamber (IC) placed at the end of the PRISMA spectrometer are discussed in Section 2.1.4 of this work. The main purpose of the detector is to perform Z identification using the previously mentioned $\Delta E - E$ method. Figure 3.6 presents a schematic view of the segmentation of the electrodes into 40 central pads and 8 side pads.

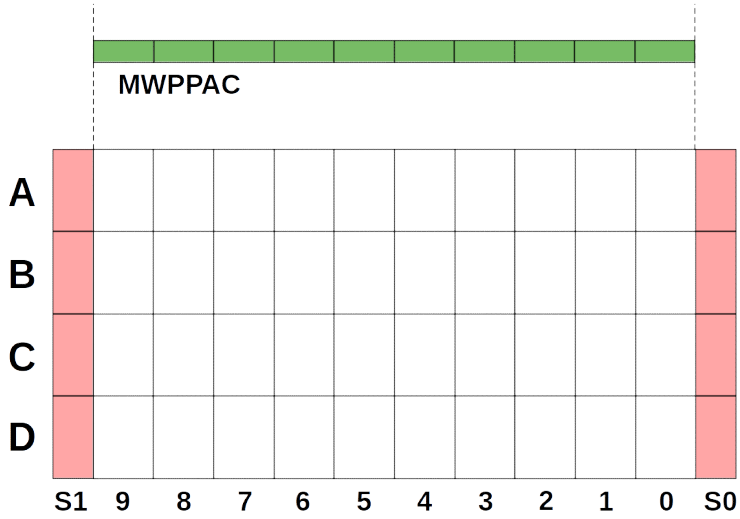

Figure 3.6: Schematic view of the Ionization Chamber (IC) of the PRISMA magnetic spectrometer.

The first stage in the calibration of the detector is the implementation of upper and lower thresholds for each of the 48 segments. This step is particularly crucial for the 8 side pads, as they are used as veto for the entire IC. Figure 3.7 shows an example of the raw energy loss spectra measured during the experiment by each of the segments corresponding to a single column. The large pedestal is due to electronic noise and has to lay below the threshold, highlighted in red, in order to be removed. While performing this procedure, it was discovered that the pads C0 and D7 did not acquire any data

during the course of the experiment. This issue was apparently caused by manufacturing defects in the construction of the IC pad in the first case and by a broken contact in the other. As a consequence, all the events where at least one pad from columns 0 or 7 was above threshold had to be removed from the rest of the analysis, resulting in a loss of approximately 23% of the statistics.

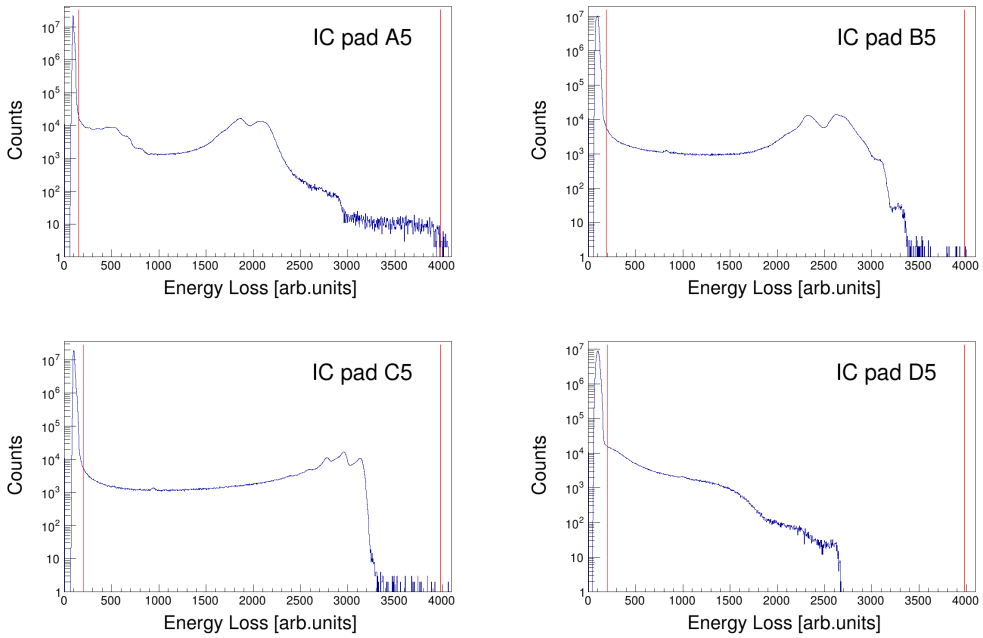

Figure 3.7: Example of the raw energy loss spectra recorded by the four pads forming a single column of PRISMA's IC. See Figure 3.6 as a reference.

To follow, the second phase is the gain matching of all of the IC pads. To achieve this, a run of calibration with a pulser was acquired. Square signals of different amplitudes were injected simultaneously in all of the IC preamplifiers and recorded through the normal data acquisition system. The result of the calibration is shown in Figure 3.8.

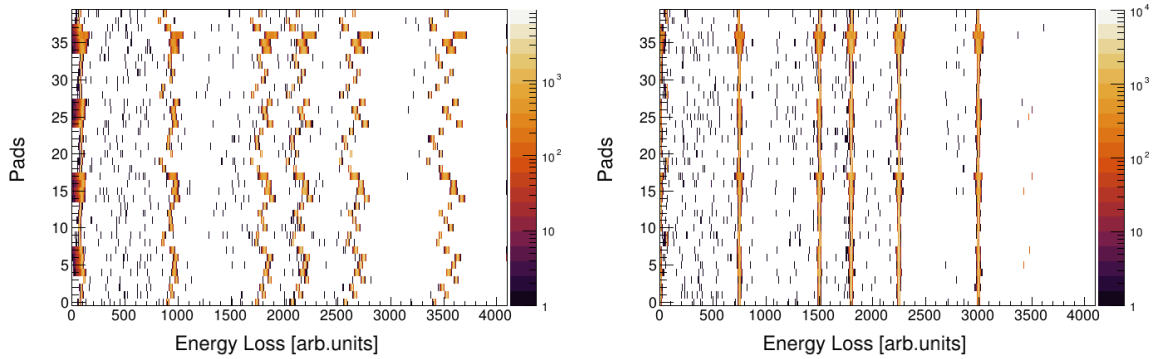

Figure 3.8: Comparison between the 40 IC pads spectra before (left) and after (right) gain matching. The data were acquired in a calibration run where a squared pulsed signal of amplitudes 25, 50, 60, 75 and 100 mV was injected simultaneously in all the IC preamplifiers. Pad numbers from 0 to 9 correspond to row A, 10 to 19 to row B, 20 to 29 to row C, 30 to 39 to row D.

The procedure, however, was not sufficient, as the total $\Delta E - E$ spectrum presented a clear misalignment between the curves corresponding to different columns of the IC, as indicated by Figure 3.9a. To obtain this plot, the first two rows of the IC were treated as ΔE layer and only events where a single column of pads was above threshold were taken into account. In order to solve the problem, two different techniques were tested in parallel. The first one involved a simple fine tuning of the

calibration parameters directly on the experimental data from the $\Delta E - E$ spectrum, resulting in the plot of Figure 3.9b. The second method, on the other hand, had a more practical approach consisting in the use of a charge injector to send a known amount of charge directly into each of the pads of the IC (see Figure 3.9c for the outcome). This technique allows to take into account possible differences among the segments, with the downside of being relatively slow and tedious, as the process has to be carried out individually for each of the pads. In conclusion, though both methods were able to solve the misalignment problem, the first one was deemed preferable from a time efficiency point of view, as the other was tested only on columns 2, 3, 4 and 5 and would have had to be repeated on the remaining six to obtain a proper calibration.

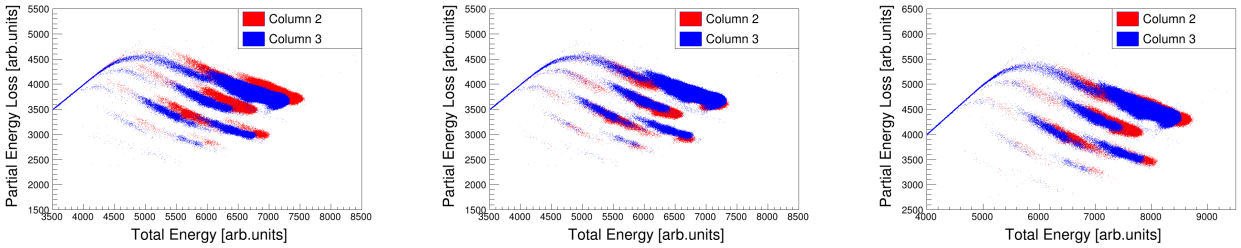

(a) Simple calibration using pulser. (b) Fine tuning of pulser calibration. (c) Calibration with charge injector.

Figure 3.9: Comparison between the single column $\Delta E - E$ plots of columns 2 and 3 of the IC obtained with three different calibrations.

During this investigation, some peculiar features of the single column $\Delta E - E$ spectra were observed. To start, the separation between the pads of the third and fourth row is clearly visible, due to the fact that a certain threshold has to be surpassed before the energy loss is recorded. In addition, moving from column 9 to 1 (Figure 3.10), the events in each band, corresponding to nuclei with the same atomic number, gradually separate, first forming two/three distinct structures and then further splitting into smaller clusters. Careful investigation was carried out after A and q identification, revealing that the main structures represent various atomic charge states, while the clusters correspond to different mass numbers, as shown by Figure 3.10.

A possible explanation for the phenomenon is that the selection of a certain column of the IC corresponds to a specific region of the focal plane which determines certain combinations of energy, mass number and atomic charge state. Indeed, the trajectory of the ions inside the dipole is regulated by the following equation (see Section 3.2.5 for a full explanation).

$$B\rho \propto \frac{A}{q}\beta \tag{3.6}$$

As the velocity β is proportional to the square root of the ions energy, the equation above implies that, assuming all of the reaction products to be scattered in the same direction going through the MCP, for a fixed combination of Z, A and q, a selection of focal plane position directly corresponds to a specific energy distribution. Consequently, different combinations of Z, A and q end up in different positions in the $\Delta E - E$ spectrum, leading to the formation of small clusters as in Figure 3.10a. This explanation, however, is not sufficient, as it does not predict the gradual broadening of the observed structures from column 1 to column 9. Indeed, the description fails to predict the evolution of the behaviour through the different columns. The cause is the wrong assumption that all recoils detected by PRISMA would scatter in the same direction, when in reality they span the full angular acceptance of the spectrometer. This implies that, assuming Z, A, q are fixed, for any given MCP entrance angle there is a theoretical energy value that would allow the ions to reach any arbitrary focal plane position.

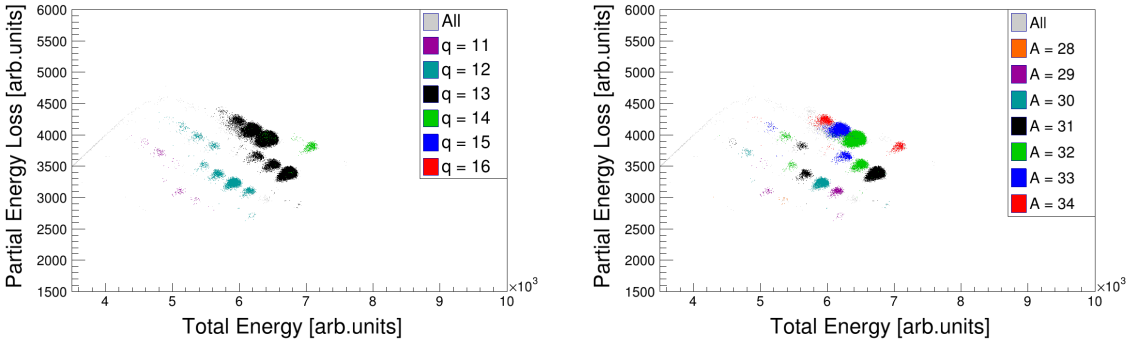

(a) Column 1 $\Delta E - E$ plots.

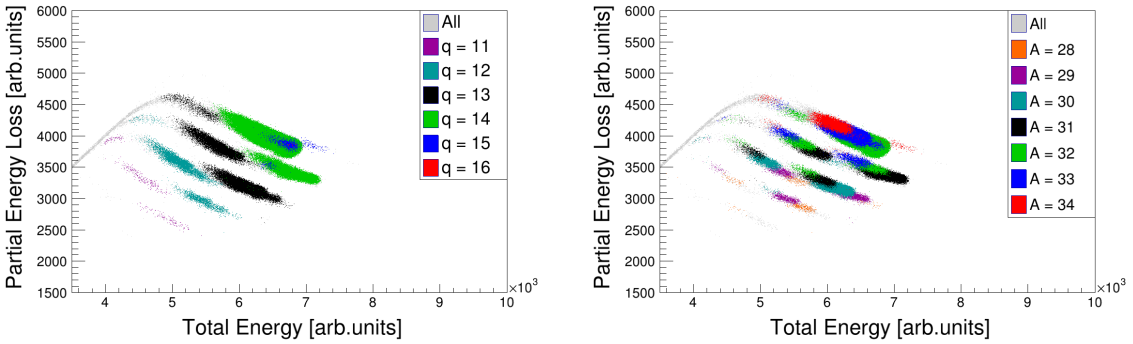

(b) Column 4 $\Delta E - E$ plots.

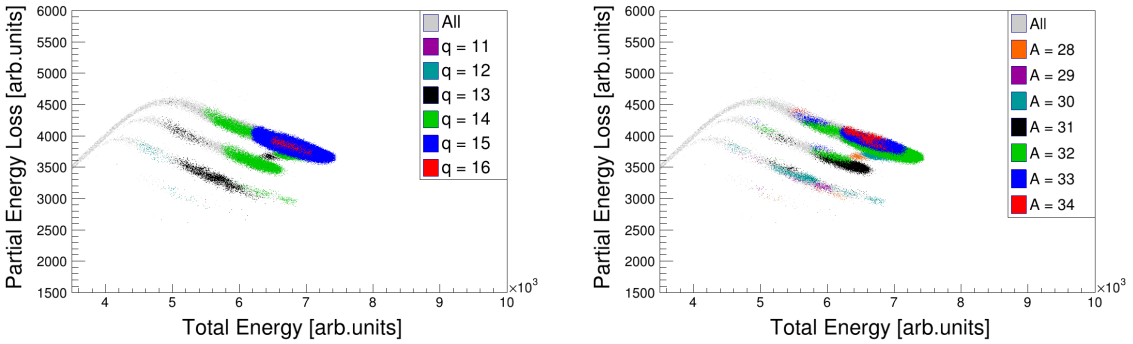

(c) Column 6 $\Delta E - E$ plots.

Figure 3.10: Single column $\Delta E - E$ plots of IC columns 1, 4 and 6. On the left panels, different charge states have been highlighted with different colors. On the right, the same procedure was applied to different masses.

As a consequence, the width of the energy distribution corresponding to a certain focal plane position should be directly correlated to the angular acceptance of the spectrometer. In reality, however, this is not always the case, as the required energy for some ions trajectories may lie outside the range of present experimental conditions. Moreover, at the start of the commissioning the magnetic field intensities are chosen in order for the main charge states of the elastically scattered ^{32}S nuclei to end up in the central region of the focal plane. These typically represent the most energetic ions, as no energy is lost through the transfer reaction process (see Section 1.4). In addition, for any given combination of Z, A, q and scattering angle, forward positions in the focal plane require higher energies while backwards positions require lower ones. Collectively, this leads to a severe restriction of the energy and entrance angle distributions for the IC columns located forward in the spectrometer, as only ions with relatively high energy and low scattering angle can reach them. Columns placed backwards, on the other hand, detect particles from a wider variety of trajectories. They can be reached by both elastically scattered higher energy ions with high scattering angle or low energy reaction products

entering the spectrometer with a lower scattering angle. This ultimately results in narrower energy distributions in forward placed IC columns and wider ones in those located backward. This effect is further enhanced in the plots of Figure 3.10 as only events with straight trajectories going through a single IC column were taken into account, leading to the behaviour observed previously.

Figure 3.11 shows the total $\Delta E - E$ spectrum obtained using the PRISMA IC. Here the first two rows of pads served the purpose of ΔE layer and only events where columns 0 and 7 were fully below threshold were taken into account. The structures related to the elements Na, Mg, Al, Si, P, S, Cl (Z ranging from 11 to 17) are clearly visible and the corresponding events were selected using 2D polygonal gates. A brief discussion about the Z resolution and overall performance of the PRISMA IC is reported in Section 4.1.2 of this work.

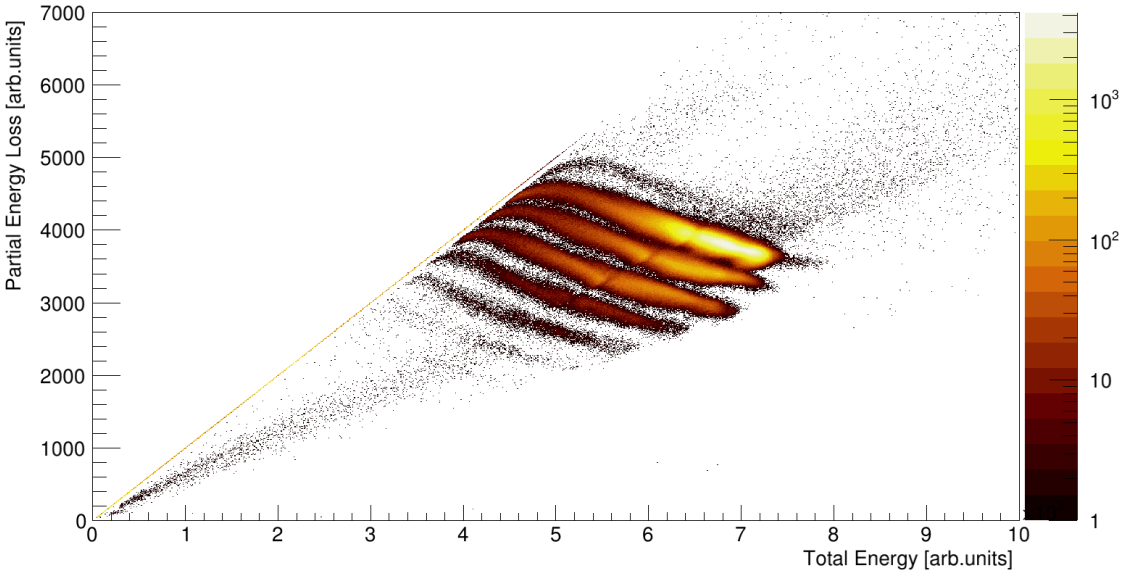

Figure 3.11: Total $\Delta E - E$ spectrum obtained from PRISMA's IC. The structures related to the elements Na, Mg, Al, Si, P, S, Cl (Z ranging from 11 to 17) are clearly visible, in accordance with previous explanation of Section 2.1.4. The corresponding events were selected using 2D polygonal gates.

3.2.4 ToF calibration

The Time of Flight of the recoils is measured between the MCP entrance detector and the MWPPAC placed at the focal plane of the spectrometer. Each section of the cathode of the MWPPAC produces a timing signal that is sent as a start to an independent Time to Amplitude Converter (TAC), while a common stop is given by the delayed signal of the MCP.

The first step in the ToF data processing is the simple conversion from arbitrary units to nanoseconds through a polynomial of degree one. In this case, thanks to the stability of the electronics, the calibration used for the spectrometer previous campaigns was already sufficiently accurate to be applied directly to the data from the present in-beam commissioning. No further operations were therefore necessary during this stage.

To follow, the ToF signals measured by the different sections of the MWPPAC were aligned between each other by adjusting their individual offset, as shown in Figure 3.12. This process is necessary in order to use the whole MWPPAC as a single detector for ToF measurement.

Once the alignment procedure is complete, a common offset is set in order to retrieve the ions correct ToF information. Estimates of the value of the parameter are obtained on a first approximation by considering the distance between the MCP and the MWPPAC detectors ($d \sim 6$ m) and the expected

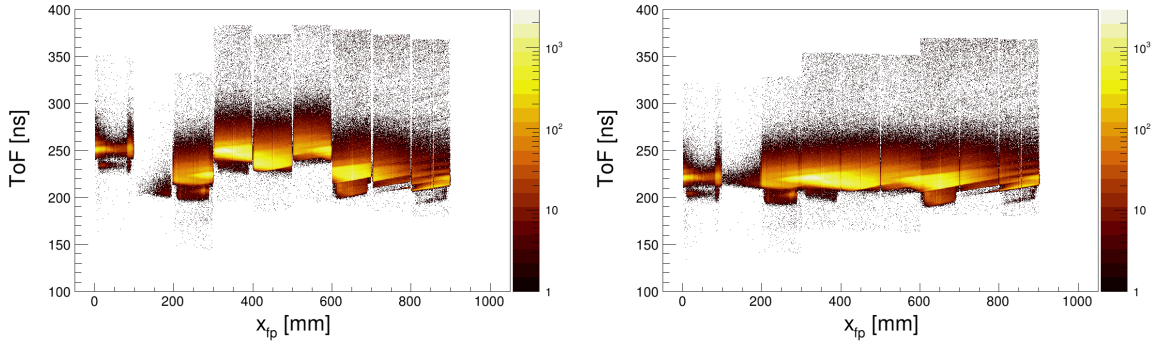

Figure 3.12: Comparison between the ToF versus x_{fp} spectra before (left) and after (right) the alignment procedure.

velocity of elastically scattered ^{32}S nuclei after taking into account the kinetic energy lost in the target ($\beta \sim 9\%$). These are compared to the experimental ToF distribution of $Z = 16$ events, previously identified in the IC using the $\Delta E - E$ method (see Section 3.2.3). A cross-check of the correct tuning of the ToF offset can be carried out at the end of the analysis by considering the energies of the gamma rays detected in the AGATA array.

3.2.5 Trajectory reconstruction

The next stage of the data processing is the event-by-event determination of the magnetic rigidity $B\rho$ of the recoils through the reconstruction of their trajectory. This is achieved using the position information coming from the MWPPAC and the MCP as well as the knowledge of the intensity of the magnetic fields of the dipole and quadrupole magnets. To simplify calculations, the trajectories of the ions are approximated as planar on the horizontal plane and ideal magnetic field geometries are assumed for the two magnets. The reaction products are assumed to start their path at the center of the target, so that the ions initial direction of motion can be easily determined. In addition, the trajectory of the recoils is assumed to be linear when outside of the magnet. Detailed discussion on the accuracy and precision of the method are show in reference [33]. Once inside the quadrupole, the magnetic field is defined by

$$\vec{B} = -\vec{\nabla} U_m \tag{3.7}$$

where

$$U_m = \frac{B_{max}}{R} xy \tag{3.8}$$

Here x, y indicate the horizontal and vertical coordinates respectively, B_{max} the maximum intensity of the magnetic field and R the inner radius of the quadrupole magnet. The force acting on the ions is then given by the Lorentz equation

$$\vec{F} = q\vec{v} \times \vec{B} \tag{3.9}$$

As the motion of the recoils takes place mainly in the z direction, their velocity can be approximated as $\vec{v} \simeq v_z \cdot \hat{u_z}$, leading to the equation of motion

$$\vec{F} = -\frac{(ze)B_{max}}{R} \begin{pmatrix} 0 \\ 0 \\ v_z \end{pmatrix} \times \begin{pmatrix} y \\ x \\ 0 \end{pmatrix} = \frac{(ze)B_{max}v_z}{R} \begin{pmatrix} x \\ -y \\ 0 \end{pmatrix} \tag{3.10}$$

The solution of the equation consists in a hyperbolic defocusing motion on the horizontal plane and a sinusoidal focusing on the vertical plane. As the trajectories of the ions are approximated as planar, only the horizontal component is taken into account.

The particles then enter the dipole magnet, which is characterized by a uniform magnetic field oriented along the vertical direction. This leads to a uniform circular motion of radius ρ in the horizontal plane, governed by the known equation

$$B\rho = \frac{p}{q} \tag{3.11}$$

Finally, the ions proceed in a straight line until they reach the focal plane detector, where their position is measured.

The algorithm enables to reconstruct the trajectory of the recoils by taking advantage of the fact that, once the entrance position and direction of motion are known, the quantity $B\rho$, also known as magnetic rigidity, completely determines the path of the ions inside the spectrometer. As a consequence, for any specific value of $B\rho$, it is possible to predict the expected position of the recoils at the focal plane detector. By minimizing the distance between the expected position and the measured one, the correct value of $B\rho$ can be deduced along with the length L of the ions trajectory from the MCP to the MWPPAC.

Once this stage of the data processing is reached, the velocity of the nuclei is calculated as

$$\beta = \frac{L}{ToF \cdot c} \tag{3.12}$$

Furthermore, starting from Equation 3.11 and taking into account the relativistic formula

$$p = \frac{mv}{\sqrt{1-\beta^2}} \tag{3.13}$$

the A/q ratio can be determined as

$$\frac{A}{q} = \frac{B\rho}{\beta} \cdot \sqrt{1-\beta^2} \cdot const \tag{3.14}$$

Since the speed of the ^{32}S ions is around $\beta \sim 0.1$, the corresponding factor $\sqrt{1-\beta^2} \sim 0.995$ can be approximated to 1, yielding the relation

$$\frac{A}{q} = \frac{B\rho}{L} \cdot ToF \cdot const \tag{3.15}$$

Here the proportionality between the A/q ratio and the ToF is evident. For this reason, the 2D matrix of A/q versus focal plane position is also used to fine tune the time alignment of the different sections of the MWPPAC. Such spectrum is displayed in the left panel of Figure 3.13, while the β distribution obtained from the experimental data occupies the right panel.

Further optimization of the trajectory reconstruction algorithm was achieved by fine tuning the effective quadrupole length and the target quadrupole distance parameters. Such procedure is necessary as the calculations performed to determine the magnetic rigidity of the ions involve a number of approximations and do not take into account the fringe fields of the magnets. As a consequence, a number of parameters are introduced in the code to represent the effective dimensions of the magnetic field regions. During this work, the quadrupole length and target quadrupole distance have been optimized through an iterative procedure around the nominal values in order to maximize the A/q resolution. Figure 3.13 shows already the results of such optimization.

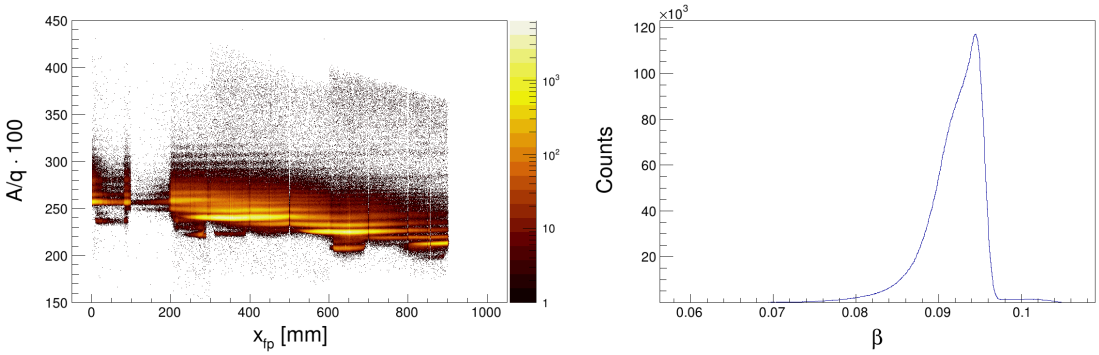

Figure 3.13: A/q versus x_{fp} matrix (left). Recoils velocity β distribution (right).

3.2.6 Charge state identification

At this stage of the analysis the nuclear charge number Z and A/q ratio are known for each of the detected ions, therefore the identification of the atomic charge state would allow to directly obtain the mass number and achieve a complete identification of the nuclei.

This task can be accomplished relatively easily, as will be proven in the next few lines of calculations. To start, let us remind 3.11 for the motion of a charged particle in a uniform magnetic field.

$$B\rho = \frac{p}{q}$$

As was shown in the previous Section, approximating to the non-relativistic regime does not lead to overly imprecise estimations. Therefore, by making use of the classical relations $p = mv$ and multiplying both sides by v, we can write

$$B\rho \cdot v = \frac{mv^2}{q} \tag{3.16}$$

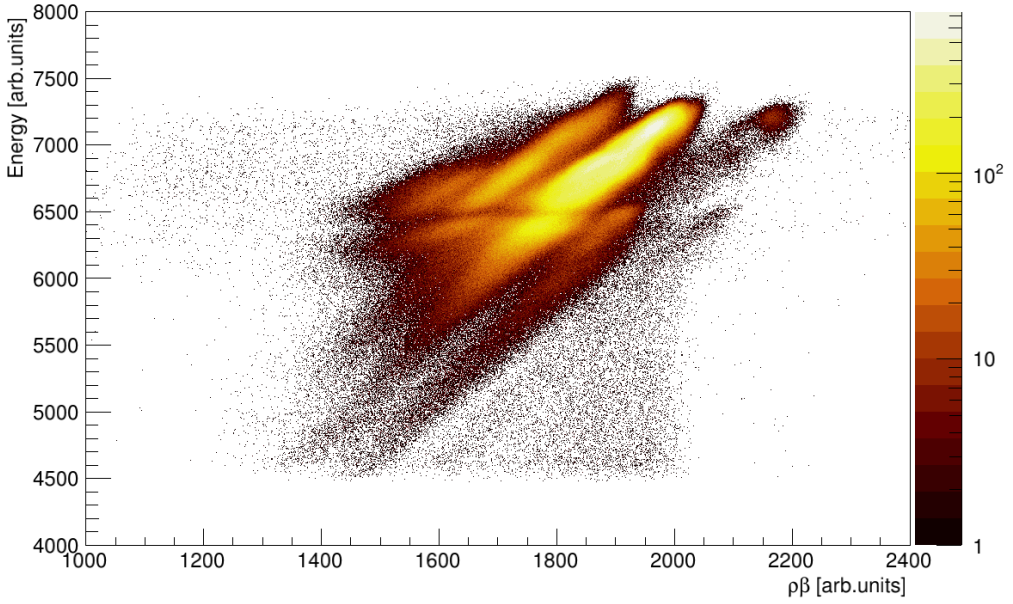

Figure 3.14: Energy of the recoils versus $\rho\beta$ spectrum for $Z = 16$. Atomic charge state identification is obtained by applying 2D polygonal gates to the band-like structures present in the plot.

We can now apply the relations $E_k = \frac{1}{2}mv^2$ and $v = \beta c$ to finally get

$$E_k \propto q \cdot \rho\beta \tag{3.17}$$

Here the kinetic energy E_k of the ions is measured by the IC placed at the end of the spectrometer, while their curvature radius ρ and velocity β are determined during the trajectory reconstruction. The charge state identification can therefore be obtained by applying 2D polygonal gates to the band-like structures of the kinetic energy versus $\rho\beta$ matrix (Figure 3.14). As the atomic number of the ions is well known at this stage, gating the events on Z, as performed in Figure 3.14, is a sensible curse of action in order to reduce unwanted background. Since the absolute value of the kinetic energy is not actually measured, the determination of the charge state corresponding to each band is achieved by comparison with software calculated estimates and later verified by the mass number identification.

3.2.7 Mass number identification

The last step in the PRISMA data processing is the event by event identification of the mass number A of the recoils detected in the spectrometer. At this stage of the analysis the ions atomic number Z, atomic charge state q and A/q ratio have been determined, therefore a simple multiplication of the last two quantities should allow to easily discern the isotopic nature of the nucleus. Due to non-linearity effects, however, the procedure does not yield the correct results. Indeed, the multiplication of the A/q spectrum gated on Z and q by the corresponding integer charge number does not generate a satisfactory mass distribution. Instead, an effective non-integer charge state is implemented. This parameter is determined by comparing the centroid of each peak of the Z and q gated A/q distribution, obtained via guassian fit, to the corresponding expected mass number. The following equation shows the nature of such comparison.

$$q_{eff} = \frac{1}{N}\sum_{i=1}^{N}\frac{A_i}{(A/q)_i} \tag{3.18}$$

Here q_{eff} represents the effective charge state, N counts the number of peaks employed in the calculation, $(A/q)_i$ is their centroid and A_i the expected mass number. The final mass distribution is therefore obtained by multiplying the A/q spectrum, gated on Z and q, by the corresponding q_{eff} parameter while integrating the statistics from all atomic number and charge state combinations.

Figure 3.15 shows the A/q spectra gated on $Z = 16$ and different values of q. In the plot corresponding to $q = 13$ an anomalous peak is present around abscissa 240. The structure is perfectly aligned with the maximum of the $q = 14$ distribution, indicating the presence of a possible contamination. It should be noted that the $q = 14$ charge state is by far the most intense, so a relatively small contamination coming from it is able to produce a significant change in the A/q spectrum of the $q = 13$ state. Moreover, the phenomenon appears to be related to the malfunctioning of pad D7 of the IC, as before the removal of column 7 this effect was much more intense. A more refined 2D gate in the kinetic energy versus $\rho\beta$ matrix (Figure 3.14) could possibly reduce contamination, at the expense of statistics. For the analysis presented in this work, it was decided to proceed with the current settings.

Figure 3.16 shows the final mass distribution gated on different atomic numbers Z. A representative value for the experimental mass resolution is $\Delta A/A \simeq 1/80$. The figure is quite poor, comparatively with previous campaigns, but sufficient for the necessities of this particular experiment. See Section 4.1.3 for a more complete discussion.

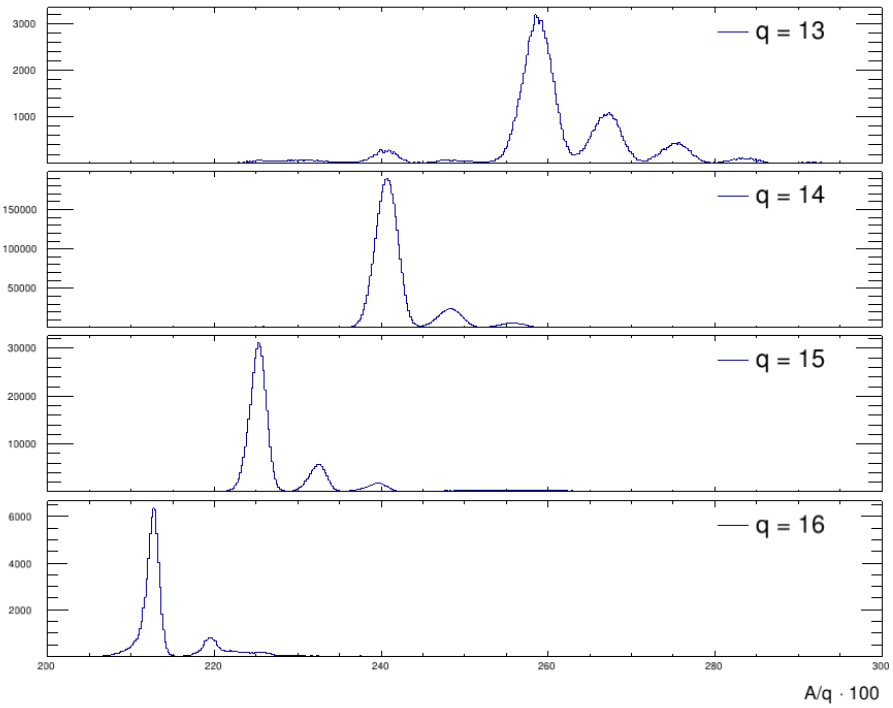

Figure 3.15: A/q distributions for different charge states of the $Z = 16$ events.

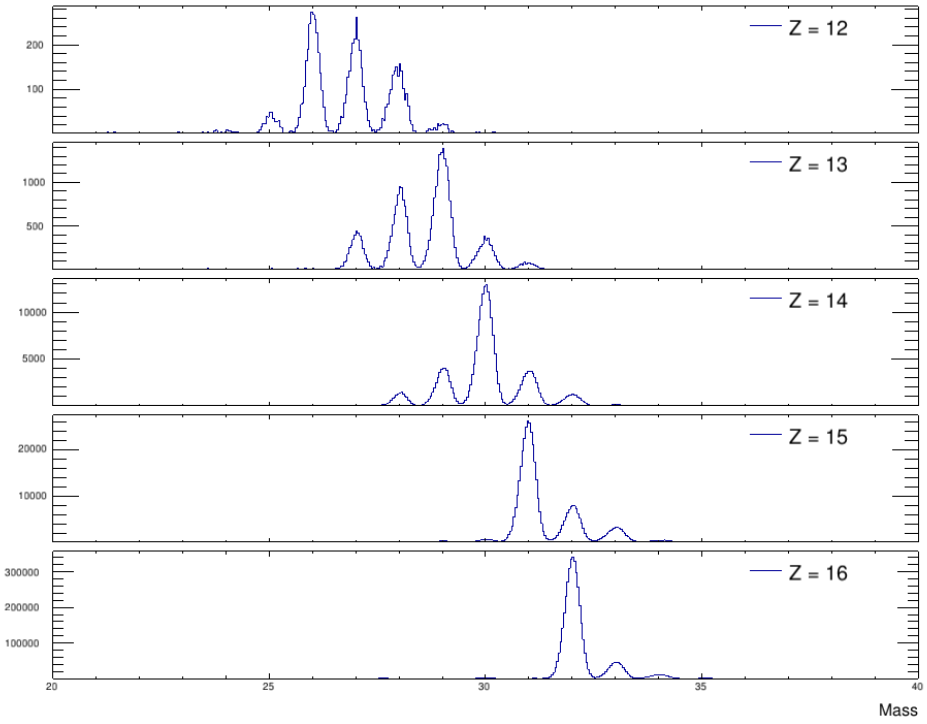

Figure 3.16: Mass distributions gated on different atomic numbers.

3.3 AGATA data processing

The main features and capabilities of the AGATA gamma array were described in detail in Section 2.2 of this thesis. Since the focus of this work is mainly on the PRISMA magnetic spectrometer, the AGATA data processing will be briefly described in this Section before moving to Chapter 4 to consider the results. A more thorough discussion about the performance of the array in its in-beam commissioning is reported in reference [34].

During the experiment, 9 AGATA ATCs were mounted on the setup, for a total of 27 segmented HPGe crystals, of which 23 operational. Each detector yields a total of 38 signals, which are divided in 36 for the segments and two for the core. The core contact is doubled as in its case two different preamplifiers with two different gains are employed.

The AGATA data processing can be divided in two main stages:

- The Local Level, where each crystal is handled separately. Here the raw signals coming from the data acquisition are processed, the energy calibration and time alignment of the different channels are carried out along with a number of corrections that increase detectors resolution. Most importantly, the reconstruction of the position of the gamma interactions inside the crystals is performed during this stage through the Pulse Shape Analysis (PSA) of the raw traces of each channel. Finally, the time alignment between the different detectors is implemented before moving to the Global Level.
- In the Global Level the full AGATA array is managed as a whole and the streams of data coming from each crystal, as well as any complementary detectors, such as PRISMA, are combined. The process involves the transition from the individual crystals frame of reference to the global frame of reference of the gamma hits positions, the implementation of a time window for gamma-gamma coincidences as well as the execution of the software that handles the data processing of complementary detectors and merging of the resulting information in the main data stream. In addition, the reconstruction of the path of the gamma rays inside the array is performed and the final output file is written in the form of a ROOT tree [35].

3.3.1 Local Level

As mentioned above, the Local Level of the AGATA data processing is characterized by the individual treatment of each crystal of the array. 23 crystals were operational during the commissioning, for a total of $23 \times 38 = 874$ channels. For each event, triggered by PRISMA's MWPPAC, the data acquisition recorded the amplitude, timestamp and complete trace of each channel though the digital electronics of the apparatus.

Preprocessing

The first step in the data processing is to retrieve the absolute energy information from the signal amplitude. In order to achieve this, calibration measurements with ^{60}Co, ^{152}Eu and ^{133}Ba radioactive sources were performed just before the start of the experiment. The linear calibration coefficients were then extracted individually from each of the 874 channels of the array.

Next comes the time alignment of the different segments to the core signal, followed by the correction of any cross talk effects, both in terms of proportional cross talk and differential cross talk. These are observed in all electrically segmented detectors when the gamma-ray energy is deposited in more than one segment and are caused by the electric coupling of different channels.

In addition, during the experiment some segments can present some problematic behaviour and be labeled as either *dead* or *unstable* depending on the type of issue. The first corresponds to segments that display either extremely noisy signals or no signals at all, while the second denotes segments whose behaviour changes with time at random, leading to multiple peaks in the energy spectrum, often with sub-optimal energy resolutions. In both cases, the issue usually lies within the electronic chain, for example due to a broken contact or malfunctioning preamplifier, and does not impede the

collection of the negative charges in the core contact. Therefore, if only one segment is problematic inside the crystal, it is mathematically possible to completely retrieve its signal as a difference between the core and the sum of all remaining segments. Unfortunately, during the commissioning, one of the four crystal excluded from the analysis presented a large number of dead segments and was therefore impossible to perform the procedure.

Pulse Shape Analysis

The next step in the AGATA data processing is the reconstruction of the gamma hit positions inside the HPGe crystal through the use of Pulse Shape Analysis (PSA) algorithms. The method consists in comparing event-by-event all the traces recorded in the detector with a labeled dataset of response functions. This was obtained through simulations and validated experimentally, as described in [4]. The algorithm performs a χ^2 minimization between the experimental data and the simulated traces (Figure 3.17) through the use of an Adaptive Grid Search [36]. The procedure ultimately allows to determine the position of the hits inside the HPGe crystals with a precision of ~ 5 mm.

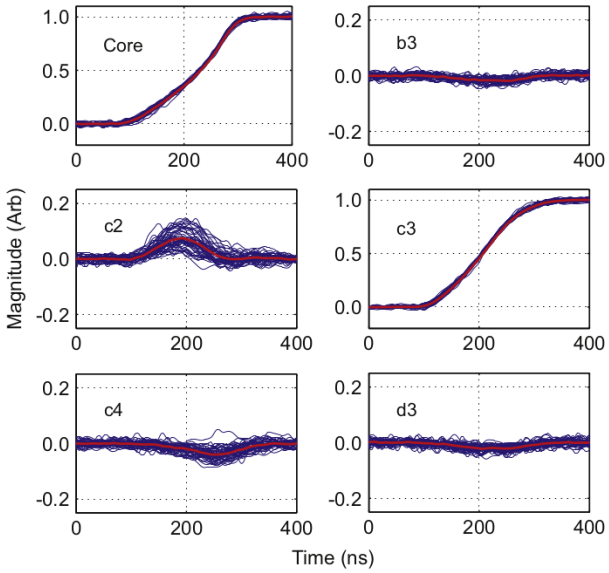

Figure 3.17: Example of the Pulse Shape Analysis showing the experimental waveforms corresponding to different segments of the crystal, overlapped with the theoretical one. Taken from reference [4].

Post PSA

After the PSA a series of refinements are implemented. These include a re-calibration of the energy that take into account the neutron damage effects thanks to the knowledge of the hits position gained in the PSA. Indeed, neutron damage is caused by localized dislocations in the germanium lattice induced by the exposition of the crystals to fast neutrons during previous experiments, causing a sub-optimal collection of the charge. The algorithm allows to partially recover the missing information, thus increasing the energy resolution. Finally, the timestamps of the cores of all the crystals are aligned between each other, in order to obtain a global time reference and avoid random coincidences.

3.3.2 Global Level

In the Global Level of the AGATA data processing, the information coming from each of the crystals as well as any complementary detectors, such as PRISMA, is merged together and additional operations, such as the gamma-ray tracking, are performed.

Event Building and Merging

The first step in the procedure is the conversion of the hits positions from the crystal reference frame to the global reference frame, taking into account the location of each detector in the apparatus.

Figure 3.18 shows the result of such operation for the current commissioning experiment. To follow, constraints on the timestamps of the hits are applied in order to accurately identify gamma-gamma coincidences. At this stage, the software handling the data processing of any complementary detectors, in this case PRISMA, is executed and the resulting measurements are merged in the AGATA stream. A time window is then applied between the AGATA and PRISMA timestamps in order to recognize coincidences between the two devices and decrease the background statistics.

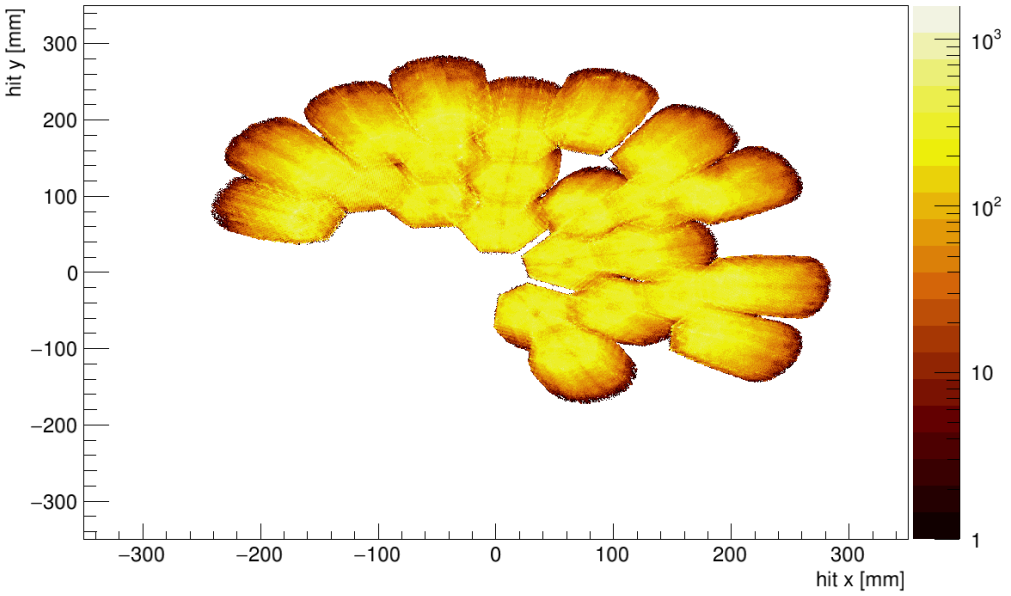

Figure 3.18: Distribution of the hit positions in the AGATA global reference frame.

Tracking

Once this stage is reached, the tracking of the gamma rays takes place. The path of the photons within the array is reconstructed using specific software developed by the AGATA community [37]. The code depends on some empirical parameters that have been determined using the previously mentioned radioactive source measurements. All the hits corresponding to the same gamma-ray trajectory are then summed in energy to the first interaction position. Figure 3.19 shows a comparison between the gamma-ray spectra obtained considering either the hits, the core signals or the tracked trajectories for both the commissioning experiment and the ^{60}Co radioactive source calibration run.

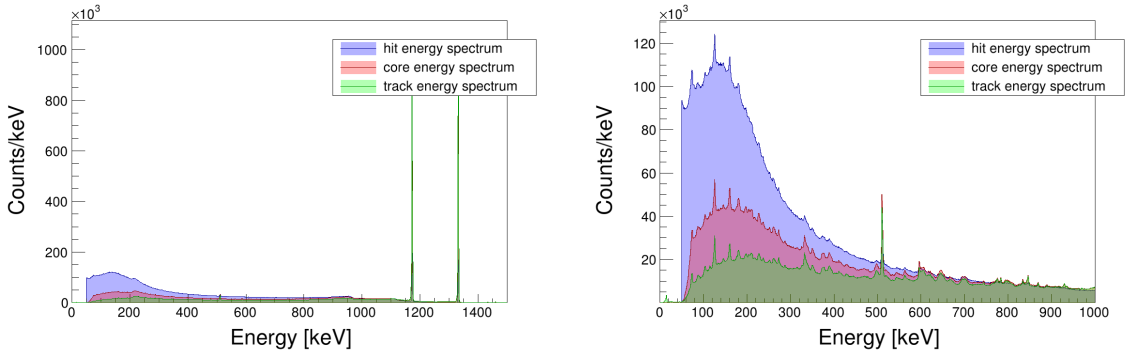

Figure 3.19: Gamma-ray energy spectra obtained in the calibration run with a ^{60}Co radioactive source (left) and in the commissioning experiment of the setup with the reaction ^{32}S + ^{124}Sn at 160 MeV (right).

From the latter, the P/T ratio in the three cases is 2.185(3)% , 17.383(12)% and 30.328(19)% respectively [34]. The absolute photopeak efficiency of the AGATA array was evaluated for the tracked

trajectories to be 3.24(9)% at 1333 keV. Moreover, the efficiency curve, parametrized through Equation 3.19, was determined for both core signals and tracked trajectories, as shown in Figure 3.20.

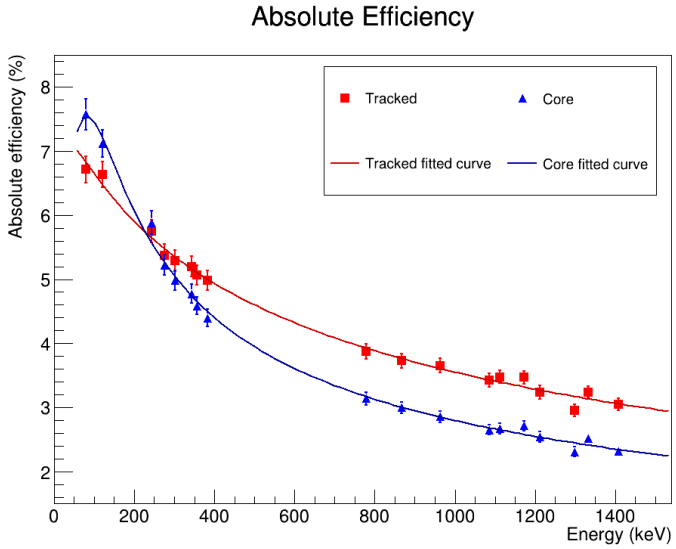

Figure 3.20: Absolute photopeak efficiency curves of the AGATA array for core signals (blue) and tracked trajectories (red). Obtained by radioactive source measurements with ^{60}Co, ^{152}Eu and ^{133}Ba. Taken from reference [34].

$$\epsilon_{ph}(E_\gamma) = \exp\left[\left((A + Bx + Cx^2)^{-G} + (D + Ey + Fy^2)^{-G}\right)^{-\frac{1}{G}}\right] \tag{3.19}$$

with $x = \ln \dfrac{E_\gamma}{100keV}$ and $y = \ln \dfrac{E_\gamma}{1MeV}$

The parameter C is fixed to 0 and G to 15. The rest of the parameters are reported in Table 3.2.

Variable	A	B	D	E	F
Core	2.18(6)	-0.50(4)	1.2(3)	-0.7(6)	-0.16(12)
Tracked	5(4)	0.1(10)	1.268(9)	-0.42(2)	-0.063(10)

Table 3.2: Parameters of the fitted efficiency curves.

To determine coincidence between the gamma rays, a time coincidence window of 100 ns was applied to the timestamps of the first hits of each track, as shown in Figure 3.21. The resulting gamma-gamma coincidence matrices for the ^{60}Co calibration run and commissioning data are displayed in Figure 3.22. In the left panel of Figure 3.22, the spectrum related to the radioactive source measurements presents some clear diagonal lines that intersect the two axis at the source emission energies. These correspond to events where the hits related to a single gamma, which released all of its energy inside the apparatus, were erroneously reconstructed by the algorithm as two distinct tracks. These structures will always appear, even in in-beam experiments with sufficient statistics and low background, as the algorithm is not perfect and in some edge cases is not able correctly infer the path of the gamma-rays inside the array.

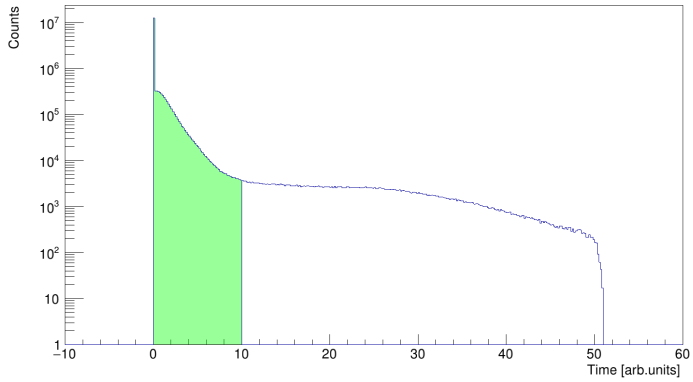

Figure 3.21: Time coincidence peak calculated among the timestamps of the first hits of each reconstructed track, with respect to the first hit of the event.

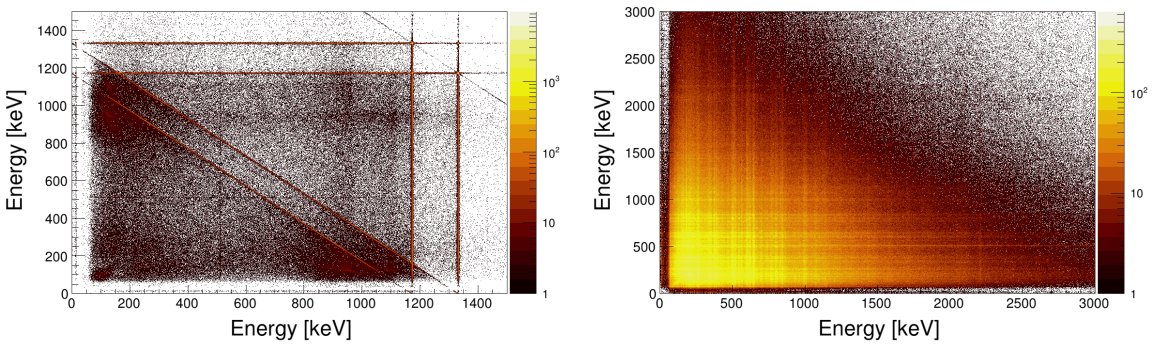

Figure 3.22: Gamma-gamma coincidence matrices obtained in the calibration run with a ^{60}Co radioactive source (left) and in the commissioning experiment with the reaction $^{32}\mathrm{S} + {}^{124}\mathrm{Sn}$ at 160 MeV (right).

Chapter 4

Results

This Chapter will discuss the main results obtained for the in-beam commissioning of the AGATA-PRISMA setup. These have been investigated in accordance with the goals of the experiment, listed in Section 1.2.

4.1 PRISMA standalone performance

As discussed in Section 1.2, part of the objectives of the commissioning experiment concerned the PRISMA magnetic spectrometer. In this Section we will assess the performance of the apparatus as a standalone device. Some of these observations were already anticipated during the data processing (Section 3.2).

4.1.1 MCP entrance detector

As shown by the right panel of Figure 3.2, the two-dimensional position distribution of the MCP entrance detector presents a region of low statistics located to the left of the cross center. The resulting shadow indicates a localized loss of efficiency, similar to what has been observed during previous experimental campaigns. This behaviour suggests that the replacement of the delay lines of the MCP detector may not have been sufficient to solve the issue. Further discussion regarding the efficiency of the MCP detector in the measurement of the position of the ions is reported in Section 4.1.4.

4.1.2 Ionization Chamber and atomic number resolution

The ability of the spectrometer to identify the recoils in terms of atomic number is one of the key features of the device and plays an essential role for understanding the good performance of the experiment both in the on-line and off-line analysis. From the spectrum of Figure 3.11, an estimate of the Z resolution of the spectrometer could be deduced. By selecting a small window of values (~ 50 channels, centered on ~ 5800) in the total energy loss (x axis) and projecting on the y axis, the effect of the inclination of the band-like structures can be neglected. The resulting distribution is shown in Figure 4.1, where the three peaks, corresponding to the atomic numbers (Z) 14, 15, 16, were each fitted with gaussian curves.

When considering any two peaks A and B, the Z resolution of the spectrometer can be estimated through the formula

$$\frac{\Delta Z}{Z} = \frac{1}{Z_{avg}} \frac{1.177 \cdot (\sigma_A + \sigma_B)}{|c_A - c_B|} \cdot |Z_A - Z_B| \tag{4.1}$$

Where $Z_{avg} = (Z_A + Z_B)/2$ is the average between the atomic numbers related to the two gaussian distributions of events, σ_i their standard deviation and c_i the corresponding centroid. The results

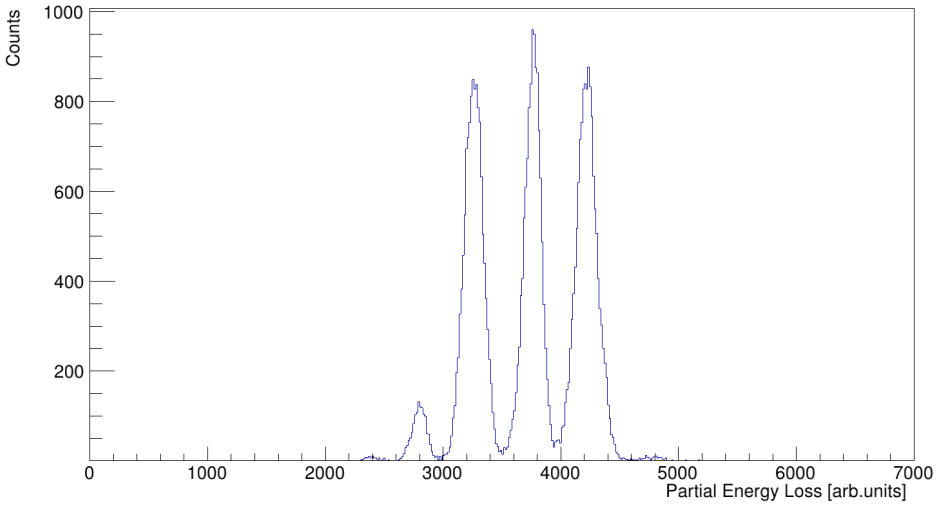

Figure 4.1: Projection along the y axis of the $\Delta E - E$ matrix of Figure 3.11, in which a small window in the x axis (~ 50 channels, centered on the value ~ 5800) was selected.

obtained with this approach depend slightly on the specific window of total energy loss values selected, as well as on the peaks chosen. As a representative figure, considering the $Z = 14$ and $Z = 15$ distributions yields an atomic number resolution of $\Delta Z/Z = 2.48\% \simeq 1/40$. This value is significantly lower than the nominal one, reported in Table 2.1. This effect could be due to the difference in mass and atomic number of the ions used to obtain the two figures. ^{32}S, in fact, is a relatively light nucleus when compared to the typical mass range of the PRISMA magnetic spectrometer ($20 < A < 150$).

Furthermore, Figure 3.10 shows that, by selecting single columns of the IC when producing the $\Delta E - E$ plots, it is possible to identify atomic charge state and mass number of the ions that induce a signal in the most forward placed IC pads, in addition to the atomic number. This effect could be very useful, especially during the online analysis, as the calibration of the IC is relatively fast and can be performed at the time of the experiment, for example to determine which transfer channels are being populated.

4.1.3 Mass resolution

Figure 3.16 shows the experimental mass spectra obtained through trajectory reconstruction in the PRISMA magnetic spectrometer. As the plots are already calibrated, an estimate of the mass resolution of the spectrometer can be obtained considering any single peak of any of the histograms. After fitting the peak with a gaussian curve, the mass resolution can be calculated simply as the ratio between the Full Width at Half Maximum (FWHM) and the centroid of the function. As with the Z resolution, the results obtained with this approach can vary slightly. For example, some peaks have tails or are inherently wider than others. Some parts of the focal plane may present a lower precision in the trajectory reconstruction, due to the quality of the selected optical parameters and approximations in the magnetic field geometry.

As a representative value, considering the $A = 32$ central peak of the $Z = 16$ mass spectrum yields a mass resolution of $\Delta A/A = 1.26\% \simeq 1/80$. Previous campaigns employing the PRISMA magnetic spectrometer showed better performance in the identification of the nuclear mass. In an experiment performed in 2009 ([38]) a beam of ^{40}Ar at 250 MeV was delivered onto a 0.3 mg/cm^2 thick ^{208}Pb target. During the experiment, PRISMA was coupled to the CLARA array of gamma-ray detectors and placed at a 54° angle with respect to the beam axis. The conditions closely resembled the current commissioning, with the exception of the much higher beam energy. At the time, the mass resolution of the spectrometer was measured to be $\Delta A/A \sim 1/150$. Further investigation is required in order to understand the causes of the performance decrease. At the time of writing, additional experiments

have all shown a similar behaviour. Nevertheless, the current mass resolution is sufficient to identify the recoils that were detected by the spectrometer during the commissioning, as their mass number did not exceed $A = 35$.

4.1.4 Partial efficiencies

In most of the experiments that involve the collision of a beam of heavy ions onto a target material, the efficiency of the detectors is one of the key factors that determine their feasibility. In the case of the current in-beam commissioning, the experiment was not designed to fully evaluate the transmission and efficiency of each element of the PRISMA magnetic spectrometer. Nevertheless, some meaningful figures that partially determine the efficiency of the device can still be calculated.

To start, let us consider that, from an experimental point of view, it is typically preferable to acquire some random events due to a low threshold or electronic noise rather than lose part of the actual statistics, as long as the acquisition rate can be handled comfortably by the system. As a consequence, the total counts acquired in the experiment include a certain amount of random noise and non-physical events. As such, it is essential to identify a number of conditions that could reduce this contamination to a negligible amount.

As a first guess, we could require at least one MWPPAC cathode signal to be within the lower and upper thresholds (see Figure 3.3 as an example). Through this condition, from here denoted *cath*, we observe a reduction of the number of events to 85.56(0.09)% of their original number, where the uncertainty was estimated through a Poissonian distribution. Among this *cath* sample, 7.62(3)% of the counts present a multiplicity larger than one in the number of cathodes firing. These could be caused both by random noise as well as real events where two recoils interacted with the detector (particle multiplicity) or a single ion passed in between two cathodes, inducing a signal in both of them (signal multiplicity).

In order to achieve a better identification of the physical events, a second condition, requiring at least one Time-of-Flight (ToF) signal to be within the thresholds defined by the user, was applied on top of the previous one. The condition, from here denoted *ToF*, causes a further reduction of the previous sample to 31.27(7)% of its original size. This large loss of statistics is rather anomalous, so further investigation has been carried out by comparing the rejected events to the ones that satisfied the requirement.

As a general result, the same behaviour was observed in both samples. The $\Delta E - E$ matrix obtained from the PRISMA IC revealed similar compositions of the recoils in terms of atomic number Z. The MCP position distribution and focal plane position spectra showed no apparent difference, even at the level of the raw signals. It is therefore unclear what caused the loss of statistics in the ToF measurement, though a possible explanation could be a problem in the analog electronics that deliver the stop signal, coming from the MCP, to the TDCs, in order to perform ToF measurement. Nevertheless, the application of both *cath* and *ToF* requirements should still increase the selectivity and allow to assume the fraction of non-physical events to be negligible for the scope of this analysis.

The partial efficiency of the MCP entrance detector in the measurement of the ions position can be obtained by considering the events that fall inside the 2D polygonal gate shown in Figure 3.2. This condition will be denoted as *mcp* and is meant to discriminate between random noise and valid counts. Real events where it was not possible to measure the MCP position are also placed outside the gate, while a small amount of noise inevitably falls inside the area as well. Unlike previous cases, here the bias introduced by the user in the procedure is more significant, so results could vary slightly. The events that satisfy the *mcp* condition form 42.46(8)% of the *cath* sample, while they account for 91.3(3)% of the data where both *cath* and *ToF* condtions are met. This large discrepancy seems to further suggest the possibility of a problem in the overall read-out of the MCP signals. Overall, the partial efficiency of the MCP entrance detector can be estimated assuming as valid the second value of 91.3(3)%, since the more stringent constraints should allow to reject non-physical events more effectively. This figure, however, represents only the performance in the position measurement and not

the overall efficiency of the device. Furthermore, let us remind of the localized loss of statistics of the MCP detector that has been observed in the plots of Figure 3.2 and discussed in Section 4.1.1. This inefficiency should be the cause for at least part of the events that do not satisfy the *mcp* requirement.

Moving the focus to the MWPPAC detector itself, similar considerations can be applied. Here the condition establishing valid position measurement, denoted *ppac*, is satisfied if any of the x_l or x_r signals (20 in total) are within the corresponding thresholds. The fraction of *ppac* events is 73.19(12)% in the *cath* sample and 77.9(2)% in the *cath* plus *ToF* sample. The difference, in this case, is not very large and could be explained simply by random counts that the higher selectivity of the second method is able to filter out. The overall partial efficiency of the MWPPAC detector in the measurement of the focal plane position of the ions can therefore be assumed to be 77.9(2)% for this specific commissioning experiment, in accordance with the previous arguments.

As shown by Figure 3.5, however, it is clear that during the experiment not all MWPPAC sections performed at the same level. Moreover, the focal plane distribution was not uniform, so an additional bias is introduced in the calculation to favor some sections with respect to others. A section-by-section evaluation of the partial efficiency was thus carried out. The *cath*, *ToF* and *ppac* conditions, at first applied requiring at least one signal to satisfy the thresholds, have now been declined considering the single section and quantities. In order to avoid possible misunderstandings, the *ppac* constraint will be denoted as *pos* when considering a single section. The condition therefore describes events where at least one of the x_l or x_r signals associated to that section is valid within thresholds, so that the quantity x_{fp}, representing the focal plane position, can be reconstructed. In addition, *left* and *right* conditions are defined for when at least one of the two x_l and x_r signals, respectively, falls inside the thresholds. Table 4.1 shows the results of the calculation.

Section	*cath*			*cath* & *ToF*		
	left	*right*	*pos*	*left*	*right*	*pos*
0	8.60(11)	9.85(12)	14.43(14)	11.1(2)	13.4(3)	19.5
1	2.67(8)	0.59(4)	3.10(9)	1.88(11)	0.44(6)	1.89(11)
2	54.1(3)	47.5(3)	58.8(3)	72.8(7)	63.8(6)	76.9(7)
3	80.9(3)	76.5(3)	88.8(3)	84.4(5)	79.2(4)	90.7(5)
4	88.4(4)	79.5(3)	92.4(4)	91.9(6)	85.3(6)	92.3(6)
5	34.1(2)	68.8(4)	70.7(4)	31.9(4)	75.3(8)	76.2(8)
6	57.3(2)	28.44(14)	63.3(2)	61.7(4)	26.0(2)	63.3(4)
7	45.1(3)	68.6(4)	72.5(4)	27.4(6)	78.9(13)	79.9(13)
8	83.6(5)	82.9(5)	88.4(5)	94.9(15)	93.4(15)	96.5(15)
9	NULL					

Table 4.1: Partial efficiencies of the different sections of the PRISMA MWPPAC (expressed in terms of percentages).

In the row related to section 9, the NULL keyword stands to indicate that no counts were recorded in the particular section. This notion is in accordance with previous observation (see Section 3.2.2) regarding the fact that no valid data was acquired by section 9 of the MWPPAC, possibly due to a broken internal contact. On the other hand, sections 0 and 1 did acquire data, however the two present a much lower position efficiencies with respect to the others, both considering the *cath* and *cath* plus *ToF* conditions. This behaviour indicates the presence of some issue either in the electronics, voltage biasing or electrical contacts. It should be noted that this pattern is not observed in the numbers of *cath* counts, which implies that the problem lies only in the position signals and not in the cathodes. In follow up experiments with the PRISMA magnetic spectrometer, the efficiency of section 1 was partially recovered by a fine tuning of the acquisition thresholds.

A general comparison among the efficiencies calculated with the *cath* and *cath* plus *ToF* conditions shows small differences between them, similarly to the behaviour of the whole MWPPAC detector. These could be caused by the simple counting of random events that the second method is able to filter

out. A specific mention is directed however at section 2, where the previous argument is probably not valid as the difference in partial efficiencies is about 20%, suggesting some other factors could be at play.

The comparison of the *left*, *right* and *pos* partial efficiencies for both groups of conditions reveals a correlation in the probability of the presence of the two signals. In qualitative terms, this means that when one signal is acquired, the second one is more likely to be measured. This effect can be proven easily by calculating the theoretical probability of either of the two quantities being present in the assumption that the two *left* and *right* conditions be independent:

$$P(pos = left \vee right) = P(left) + P(right) - P(left) \cdot P(right) \tag{4.2}$$

The results of the calculation significantly vary from the experimental *pos* partial efficiencies of Table 4.1, indicating the two signals are actually correlated, as one would expect.

4.1.5 Maximum sustainable rate

As discussed in Section 1.2, the IC electronics and the VME read-out system of the PRISMA magnetic spectrometer have been completely refurbished since its last period of activity. Before the commissioning experiment, an assessment of the rate performance of the acquisition chain has been carried out. The test involved the use of a source of gamma radiations and an array of LaBr scintillators to serve as a trigger for the read-out system. The procedure yields an upper limit for the maximum sustainable counting rate, as the intrinsic dead time of the detectors due to physical processes is not taken into account. Figure 4.2 shows the behaviour of the dead time for different values of trigger rate.

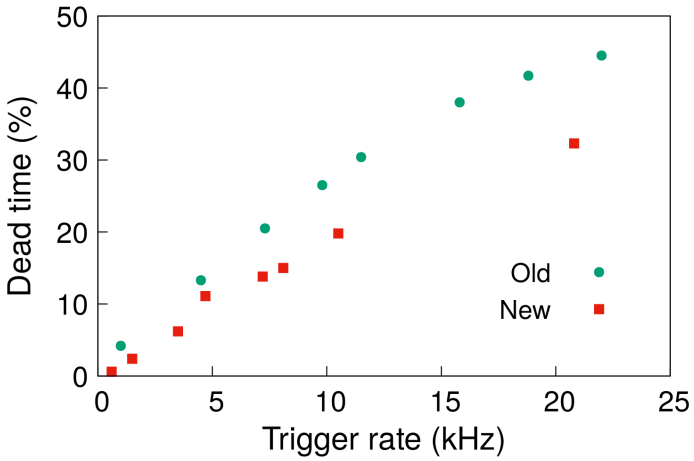

Figure 4.2: Rate capabilities of the read-out system of the PRISMA magnetic spectrometer. These were obtained before the experiment using a radioactive gamma-ray source and a LaBr scintillation detector as a trigger.

During the in-beam commissioning of the apparatus, the maximum trigger rate observed in PRISMA was approximately $\sim$ 3.5 kHz. Referring to Figure 4.2, the corresponding dead time percentage would be very small ($\sim$ 5%). Indeed, no statistical difference was observed between the trigger and acquisition rates during the experiment.

4.2 Doppler correction and coincidence

At the end of the PRISMA data processing (Section 3.2) the atomic and mass numbers (Z and A respectively) of the recoils have been determined on an event by event basis along with their velocity vector $\vec{\beta}$. This result has been achieved through the reconstruction of the ions trajectory inside

the spectrometer and the implementation of the $\Delta E - E$ technique in the spectrometer ionization chamber. Since the cathodes of the MWPPAC detector served as a trigger for data acquisition during the experiment, the gamma rays detected by AGATA were associated to each event through a time-coincidence window. Thanks to the unique features of the array, in the data processing (Section 3.3) the position of each hit inside the HPGe crystals was established using *Pulse Shape Analysis* algorithms with a precision of approximately ~ 5 mm. The path of the gamma rays inside the apparatus was then reconstructed by the *Tracking* algorithm on an event by event basis. A number of additional operations were also performed in the AGATA data processing to increase the resolution of the apparatus by correcting for various effects, which would otherwise decrease the performance of the array. Moreover, the two streams of data were merged to create a single output file.

4.2.1 AGATA-PRISMA time-coincidence

During the experiment, a time-coincidence window of about ~ 1.8 μs between the signals coming from the two apparatuses was employed to select the ion-gamma events. This was further refined in the analysis, in order to reduce the background in the gamma-ray spectra. Figure 4.3 shows the time-coincidence peak along with the improved 90 ns wide coincidence window, highlighted in green, applied later in the analysis. The peak presented a FWHM of 36 ns and its ratio over background was evaluated to approximately 1.823(2).

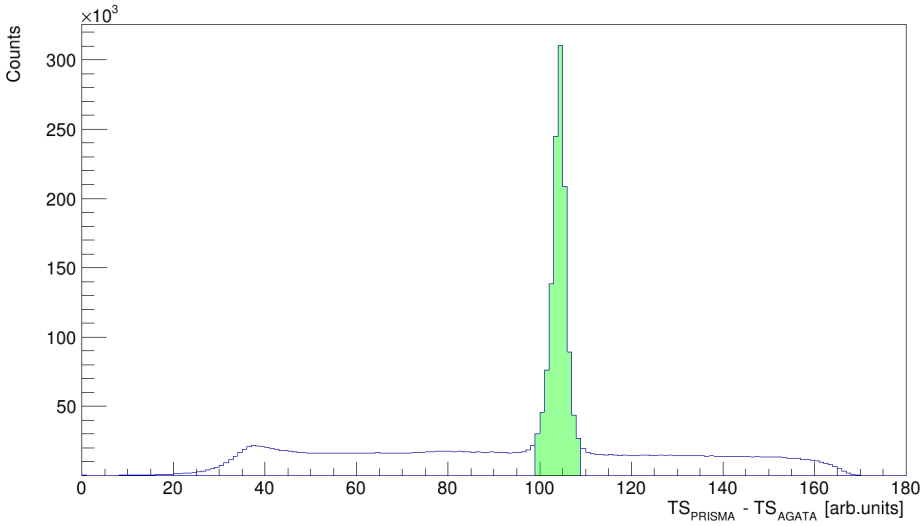

Figure 4.3: Time-coincidence peak between the PRISMA magnetic spectrometer and the AGATA array. A more refined coincidence window (highlighted in green) was applied in the analysis in order to reduce background.

4.2.2 Recoil Doppler correction

As explained in Section 1.1, the coupling of the PRISMA magnetic spectrometer to the AGATA array brings a number of advantages, namely the ability to select the transfer reaction channel by gating events on atomic and mass numbers as well as achieving event-by-event Doppler correction thanks to the measurement of the velocity vector of the recoils. The latter, in particular, is performed in accordance with Equation 1.8, as discussed in Section 1.5.

The angular resolution of the PRISMA entrance detector is approximately $\sim 0.2°$, as explained in Section 2.1.1. This value is obtained by comparing the position resolution of the device to its distance from the target, where all reactions are assumed to take place in its center. Similarly, the angular resolution of the AGATA array can be estimated to be about $\sim 1°$, taking into account the PSA position resolution and an average among the whole HPGe shell region for the distance from the target. This figure is extremely low in the field of gamma-ray detection as it is a key feature of the

new HPGe segmented crystals technology. Still, as the passage of charged particles is generally easier to detect in this range of energies, the angular resolution of PRISMA is five times smaller than the one of AGATA, meaning the uncertainty in the θ angle between the recoils and gamma-ray trajectories is completely dominated by the AGATA contribution. Moreover, the excellent performance of the array in terms of efficiency and peak-to-total ratio further increase statistics and decrease background.

As an example, Figure 4.4 shows the Doppler corrected gamma-ray spectrum of the ^{33}S recoils. A full discussion in regards to the energy resolution of the setup is carried out in Section 4.2.4 of this work.

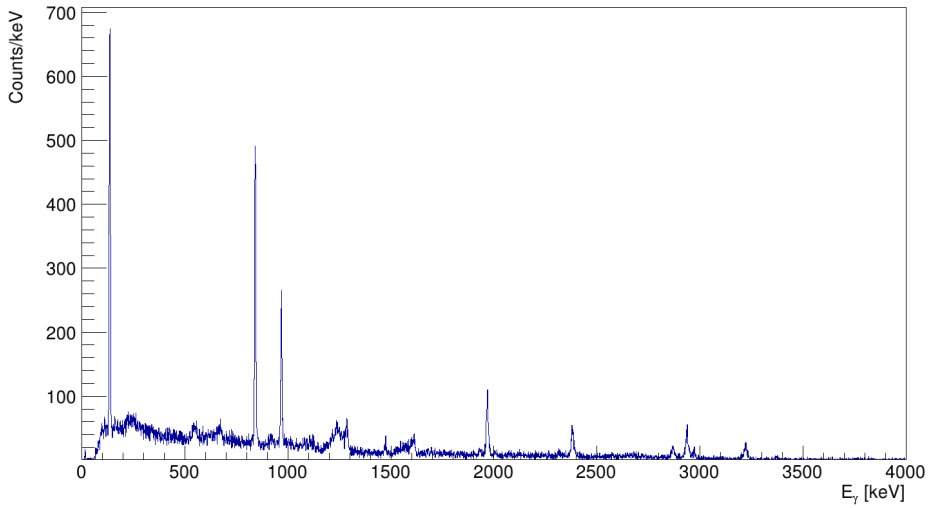

Figure 4.4: ^{33}S Doppler corrected gamma-ray spectrum.

4.2.3 Binary-partner Doppler correction

In order to perform the binary-partner Doppler correction of the gamma-ray spectra, the velocity vector of the target-like reaction products has to be determined through the full kinematic reconstruction of the two-body reaction. This requires accurate knowledge of the beam energy and target geometry as well as velocity vector of the beam-like recoils. A more detailed description of the procedure is discussed in Section 1.5 of this work. Through the calculations, the Q value of the reaction is also determined.

As an example, Figure 4.5 shows the Doppler corrected gamma-ray spectrum of the ^{123}Sn binary partner. A full discussion in regards to energy resolution is carried out in Section 4.2.4 of this work.

4.2.4 Energy resolution of the AGATA array when in combination with PRISMA

Arguably the main objective of the AGATA-PRISMA setup is its experimental application in the field of high-resolution gamma-ray spectroscopy. That being the case, energy resolution is one of the key characteristics that determine the overall performance. By itself, energy resolution in the gamma-ray detection of the AGATA array assumes the typical values of state of the art HPGe detectors, on the order of 3/1000 at 1333 keV. In experiments that involve the PRISMA spectrometer the recoils must leave the target in order to trigger the acquisition of the event and be identified. Prompt gamma-ray production therefore takes place in mid-flight conditions. For relatively thin targets, like in the current case, the same occurs for the target-like binary partners. Doppler correction is thus necessary to retrieve the energy of the detected gamma rays. The process requires the knowledge of the relative angle between the nuclei and gamma-rays trajectories at the time of the emission, as well as the speed of the ions. Section 1.5 of this work describes in detail how to perform this calculation and achieve Doppler correction. The procedure, however, introduces a number of additional uncertainty contributions to the final energy. Indeed the angular resolution of the two apparatuses as well as the accuracy in the determination of the ion velocity play an important role in the ability to achieve a

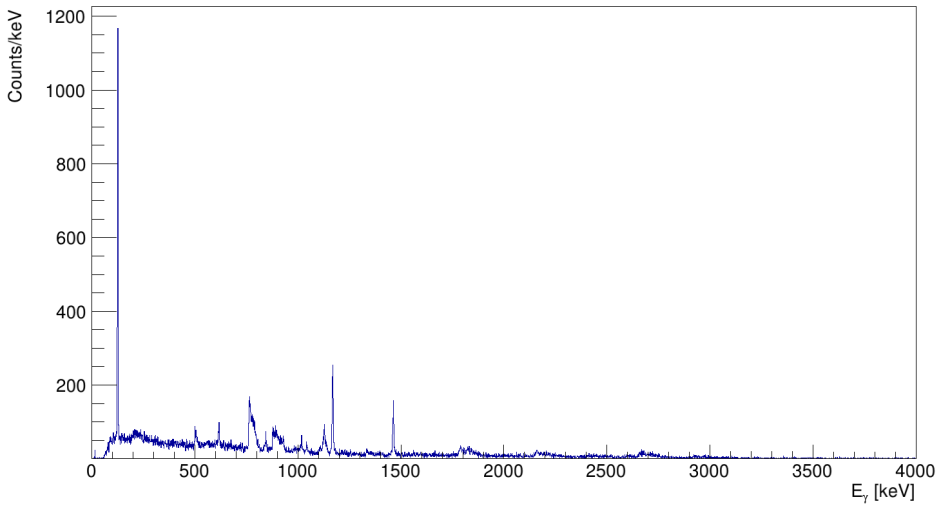

Figure 4.5: ^{123}Sn Doppler corrected gamma-ray spectrum.

high-quality Doppler correction. In addition, in the case of the target-like partners, the speed of the nuclei is calculated through full kinematic reconstruction that take into account the energy lost inside the target material. The calculation assumes all reactions to take place in the middle of the target, as it is not possible to determine the real position on an event-by-event basis. As a result, a lower energy resolution may be observed for the heavy partners of the reaction, though their lower velocity should decrease the Doppler effect. Figure 4.6 shows the behaviour of the energy resolution with respect to the gamma-ray energy for the AGATA standalone array, beam-like recoils in the AGATA-PRISMA setup and target-like recoils.

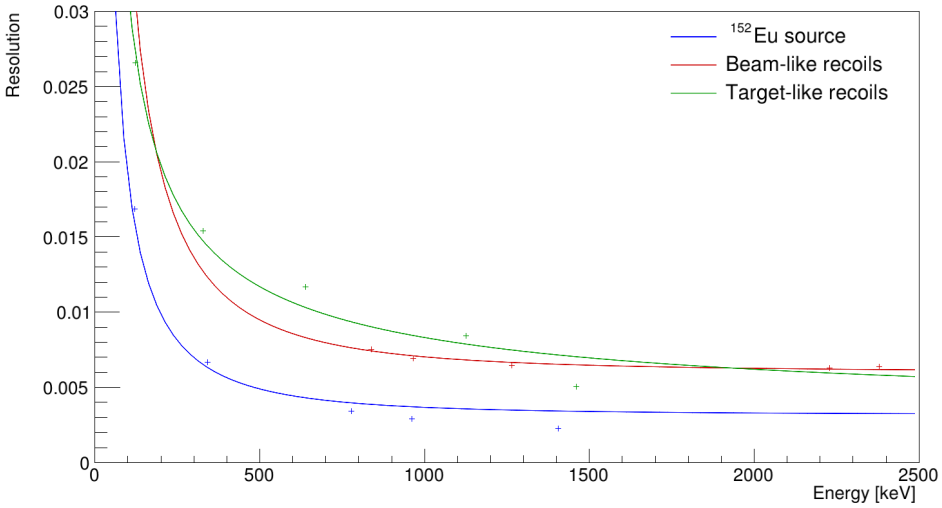

Figure 4.6: Energy resolution of the setup for source measurements with AGATA standalone (blue), beam-like recoils (red) and target-like recoils (green). Error bars are contained within the points.

The data points where obtained by fitting with gaussians some of the most intense and clear peaks in the energy spectra acquired for the ^{152}Eu radioactive source calibration (for AGATA standalone) and commissioning experiment (for the Doppler corrections). A fit of the plots with the function of Equation 4.3, taken from [30], was performed in order to recover the overall trend.

$$\frac{\Delta E}{E} = \sqrt{\frac{a}{E^2} + \frac{b}{E} + c} \tag{4.3}$$

The results clearly show that for gamma rays emitted in-flight the energy resolution after Doppler correction can never be as good as that for gamma rays emitted by stopped ions, as expected. Comparison between the beam-like and source measurement curves yields on average a decrease in the resolution by about a factor of 2. In the case of the target-like recoils, the limited number of points does not allow to estimate the contribution of the kinematic reconstruction on the overall precision of the measurement.

4.2.5 Selection in Total Kinetic Energy Loss (TKEL)

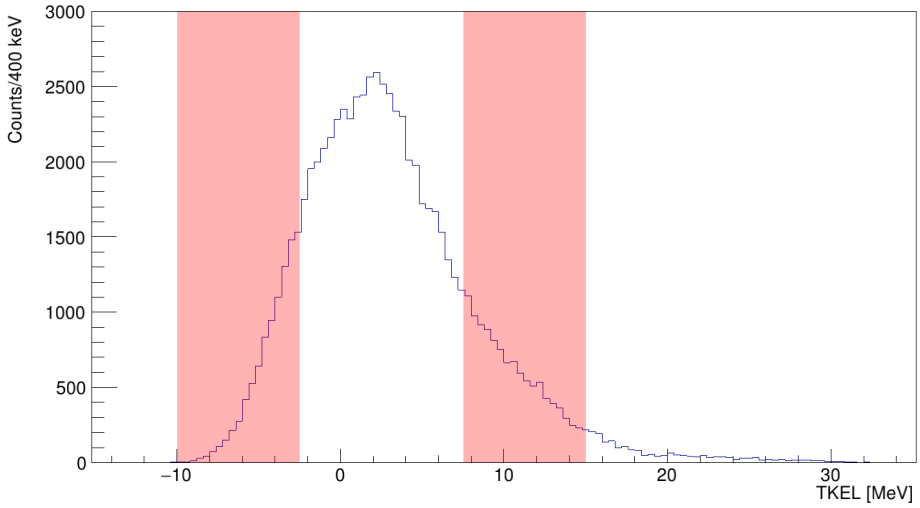

(a) TKEL distribution for the +1n transfer channel.

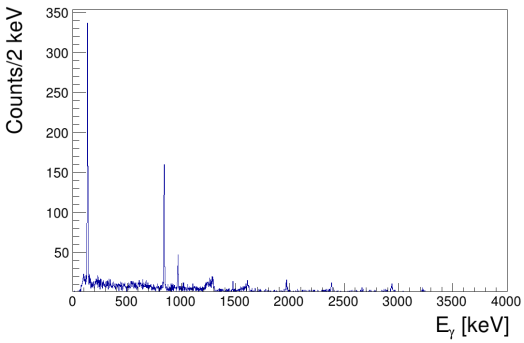

(b) ^{33}S Doppler corrected energy spectrum gated on low values of TKEL (see top panel).

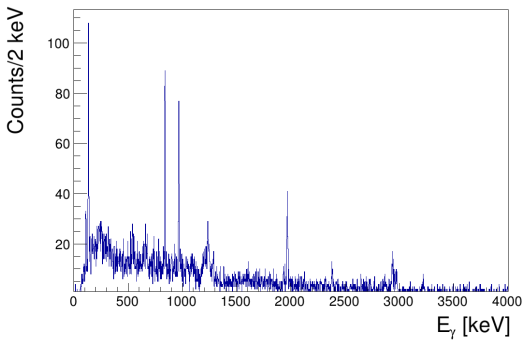

(c) ^{33}S Doppler corrected energy spectrum gated on high values of TKEL (see top panel).

Figure 4.7: Effect of TKEL selection to the gamma-ray energy spectrum in the case of the ^{33}S nucleus. (Top) TKEL distribution for the +1n transfer channel, with gates for low and high values regions highlighted in red. (Bottom left) ^{33}S Doppler corrected energy spectrum gated on low values of TKEL. (Bottom right) Doppler corrected energy spectrum gated on high values of TKEL.

The full reconstruction of the kinematics of the interaction was originally performed in order to obtain the Doppler correction related to the target-like binary partner. The procedure, however, yields in addition the Total Kinetic Energy Loss (TKEL) and Q value of the reaction, as seen in Section 1.5. The precision of the measurement is relatively low, on the order of a few MeV. The reasons of this relatively large value reside in a number of experimental limitations. Specifically, the finite thickness of the target introduces a spread in the kinetic energy of the ions detected by the PRISMA spectrometer. This phenomenon is caused by the different energy losses experienced by recoils produced near the entrance or exit of the target. This effect is not taken into account in the kinematic reconstruction, as all reactions are assumed to take place in the middle of the target. Through simple calculations, performed with the LISE++ code [39], the effect was estimated to account for an approximate spread

of 4.1 MeV in the kinetic energy of the beam-like recoils between the entrance and exit of the target for the elastic channel. Moreover, in reference [33], the resolution in velocity of the PRISMA trajectory reconstruction algorithm was evaluated to be approximately 2.1%.

Nevertheless, coarse knowledge of the TKEL of the reaction on an event-by-event basis is already sufficient to distinguish, to some degree, between gamma-rays produced by high-lying and low-lying excited states transitions, as discussed in Section 1.6 of this work. Indeed, for any specific heavy-ion reaction, the TKEL is directly correlated with the excitation energy E_{ex} of the products, as expressed by the Equation 4.4.

$$TKEL = E_{ex} - Q_{gs} \tag{4.4}$$

where Q_{gs} is the ground state to ground state Q value of the reaction. The method can be optimally applied when the difference in energy between the high-lying and low-lying states is at least on order of $\sim$ 1 MeV. As an example, Figure 4.7 shows the TKEL distribution of the one-neutron pick up channel in the current commissioning experiment, along with the Doppler corrected energy spectra, for beam-like recoils, gated on low and high regions of TKEL, highlighted in red in the first plot.

By comparing the Figures 4.7b and 4.7c, one can see that the transitions $7/2^- \rightarrow 5/2^+$ at 967 keV, $5/2^+ \rightarrow 3/2^+$ at 1967 keV, $7/2^- \rightarrow 3/2^+$ at 2934 keV and $7/2^+ \rightarrow 5/2^+$ at 2969 keV are enhanced in the second picture, while the lower energy $1/2^+ \rightarrow 3/2^+$ at 841 keV appears suppressed to some degree. This behaviour is in accordance with the level scheme displayed in Figure 4.8 (data from [40]).

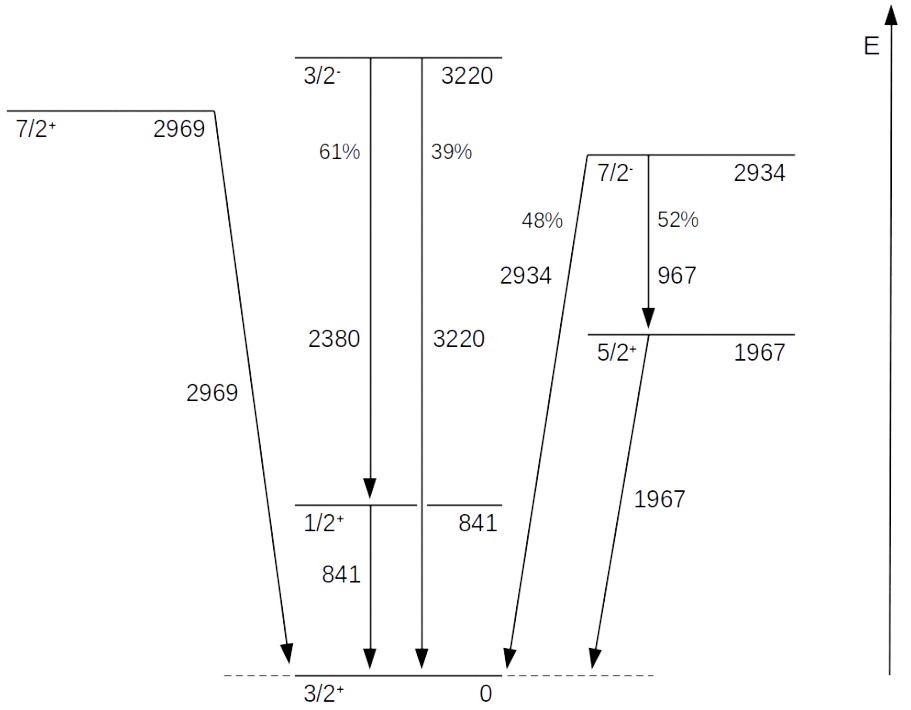

Figure 4.8: ^{33}S simplified level scheme.

Indeed, the $1/2^+ \rightarrow 3/2^+$ transition at 841 keV decays directly to the ground state, so the $1/2^+$ state is the first to be populated for low values of TKEL. Once the experimental TKEL increases, the higher-lying excited states $5/2^+$ at 1967 keV, $7/2^-$ at 2934 keV, $7/2^+$ at 2970 keV and $3/2^-$ at 3220 keV become gradually more populated in order of ascending energy. Noticeably, not all decays lead directly to the ground state, as in the case of the transitions $7/2^- \rightarrow 5/2^+$ at 967 keV and $3/2^- \rightarrow 1/2^+$ at 2380 keV. These induce the feeding of lower-lying excited states, causing the emission of their corresponding gamma rays even at higher energies. Still, the suppression of the $1/2^+ \rightarrow 3/2^+$ transition for higher values of TKEL is consequence of the lower cross section of the excitation to the $3/2^-$ state as well as branching ratio of the feeding with respect to the direct population of the 841

keV level. This same behaviour is present in the $5/2^+$ state at 1967 keV, though more difficult to observe. In this case, the energy gap between the $7/2^-$ and $5/2^+$ state is 967 keV, so the effect is less noticeable even though the branching ratio composition is similar in the two cases.

Overall, the technique finds ample use, for example, in experiments on lifetime measurement, where the removal of the feeding from higher-lying states is critical to obtain accurate results.

Chapter 5

Conclusions

In the field of high-resolution gamma-ray spectroscopy, the coupling of large acceptance magnetic spectrometers to large gamma arrays for coincidence measurements is a powerful tool for studying nuclear structure near the valley of beta-stability. Multi-Nucleon Transfer (MNT) reaction studies in high intensity stable beam facilities populate a number of moderately exotic channels with relatively high cross section. These experiments take advantage of the selectivity of the magnetic spectrometer for the identification of the reaction channel. Moreover, the measurement of the velocity vector of the heavy recoils by trajectory reconstruction is critical to perform high-quality Doppler correction of the gamma-ray energy. Consequently, at the INFN - Legnaro National Laboratories (LNL), the large acceptance magnetic spectrometer PRISMA has been recently coupled to the Advanced GAmma-ray Tracking Array (AGATA), a device that currently represents the state of the art in gamma-ray detection due to its unprecedented performances in terms of angular resolution, energy resolution, efficiency and peak-to-total ratio. A first in-beam commissioning has been carried out to evaluate the capabilities of the complete system. In this thesis, the performance of the AGATA-PRISMA setup is evaluated by using a MNT reaction $^{32}\mathrm{S} + {}^{124}\mathrm{Sn}$ at 160 MeV on a 0.5 mg/cm^2 thick target.

Concerning the PRISMA performance, main objective of my thesis work, the following conclusions can be drawn:

- A localized loss of efficiency was observed in the position distribution recorded by the Micro-Channel Plate (MCP) entrance detector. The pattern matches observations from previous experimental campaigns, indicating that the replacement of the delay lines of the device was seemingly not sufficient to solve the issue.

- The performance of the Ionization Chamber (IC) of the spectrometer after the refurbishment of the electronics and VME read-out system was evaluated. Two of the 40 electrode pads of the device appeared missing and were removed from the analysis, causing a reduction in the overall statistics. The gain matching of the various channels was performed with two different methods, as the simple calibration with a pulser was found to be inadequate. The first method relied on the fine tuning of the parameters directly on the $\Delta E - E$ matrices obtained considering single columns of the IC. The second procedure on the other hand, involved the use of a charge injector directly connected to the pads. Both techniques were deemed successful, though the first was selected for this analysis.

- As the IC employs the $\Delta E - E$ technique to determine the nuclear charge of the reaction products, the resolution in atomic number had to be estimated. A representative figure of about $\Delta Z/Z = 1/40$ was established regarding the current experimental conditions. The value is only slightly below previous performances, so further investigation may be needed, possibly with heavier systems, to evaluate the accuracy of the result.

- Distinctive structures were observed in some of the $\Delta E - E$ matrices produced for the single columns of the IC. These were determined to be associated to different atomic numbers and

charge states, suggesting the possibility to use the technique to monitor the population of transfer channels during the experiment on-line analysis.

- The mass spectrum of the recoils was determined through trajectory reconstruction and charge state identification. The mass resolution of the spectrometer was estimated to about $\Delta A/A = 1/80$. The figure is significantly worse than previous experimental campaigns. Further investigation is encouraged to assess the cause of such decrease in resolution.

- Partial efficiencies were extracted for different sensitive components of the PRISMA spectrometer, indicating a sub-optimal performance in few sections of the MWPPAC and potentially a significant loss of statistics due to the timing signals produced by the MCP. Both matters should be examined carefully to find the cause of the issues. The partial efficiencies of the MCP and MWPPAC detectors in the measurement of the ions position was estimated to be respectively 91.3(3)% and 77.9(2)% in the current configuration. Both figures could increase significantly by solving the issues mentioned above.

- The maximum rate capabilities of the new read-out system were assessed before the commissioning, estimating 10% of dead time at 5 kHz. Comparable performances were observed during the in-beam experiment where an average rate of ~ 3.5 kHz was established.

With respect to the coupling with AGATA and the performance of the complete setup, the following evidences emerged:

- The time-coincidence spectrum between the timestamps of the two apparatuses was produced. The Full Width at Half Maximum (FWHM) of the coincidence peak was evaluated to about 36 ns along with a ratio over background of 1.823(3). A more selective time-window, 90 ns wide, was then applied around the coincidence peak to remove statistical background.

- Doppler correction of the gamma-ray spectrum was accomplished considering the velocity vector of the beam-like recoils, determined inside the PRISMA spectrometer through trajectory reconstruction and time-of-flight measurement.

- A second Doppler correction was achieved considering the target-like partners, by calculating their velocity vector through the kinematic reconstruction of the interaction, taking into account energy loss in the target material. The procedure enables as well to estimate the Total Kinetic Energy Loss (TKEL) of the reaction.

- The gamma-ray energy resolution of the setup was calculated in regards to a calibration run with a ^{152}Eu radioactive source (AGATA standalone performance), as well as the Doppler corrections for both beam-like and target-like partners. As representative figures, the resolution was established for 1 MeV gamma rays to be about 0.35%, 0.7% and 0.85% in the three cases respectively. A more detailed plot of the overall behaviour is reported in Figure 4.6 of this work. No definitive difference between the precision of the beam-like and target-like Doppler corrections was observed. The analysis of the data acquired with the thicker 2.5 mg/cm^2 target of ^{124}Sn may allow to assess the contribution of the target thickness on the quality of the kinematic reconstruction and uncertainty in the measurement.

- Selection in TKEL of the gamma-ray spectrum of the ^{33}S recoils was performed to evaluate the capabilities of the setup in the statistical identification of transitions originating from either high-lying or low-lying excited states. Conditions on the values of the TKEL, related to the excitation energy, were imposed to study the corresponding gamma-ray energy distribution. The suppression of transitions from high-lying states for low TKEL values was successfully verified. The opposite was observed in the high TKEL region, though taking into account of the feeding of lower states in accordance with the level scheme of ^{33}S was necessary. The viability of the technique in the case of thicker targets could be established through the analysis of the data acquired with the 2.5 mg/cm^2 target of ^{124}Sn.

Further improvements on these studies could be gained by a multiparametric optimization of the

Doppler correction, to take into account potential small offsets in the two apparatuses positions and angles of rotation as well as measurement of the time of flight of the recoils inside the PRISMA spectrometer. The analysis of the data acquired with the ^{32} beam on the thicker 2.5 mg/cm^2 target of ^{124}Sn could also be beneficial to assess the contribution of the effective target thickness on the quality of the kinematic reconstruction and TKEL selection. Furthermore, the study of the runs performed at the start of the commissioning, regarding the reaction ^{58}Ni + ^{197}Au at 225 MeV, could allow to obtain a different set of measurements for the partial efficiencies of the PRISMA sensitive components when detecting the heavier nuclei. Finally, since the transmission of the spectrometer is not known precisely as it varies significantly over the experiments, the addition of small silicon detectors inside the reaction chamber to act as monitors like in previous experimental campaigns would allow to measure more easily the absolute transfer cross section of the various reaction channels.

Bibliography

[1] I-Yang Lee. "The Gammasphere". In: *Nuclear Physics A* 520 (1990), pp. 641–655.

[2] J Simpson. "The Euroball Spectrometer". In: *Zeitschrift für Physik A Hadrons and Nuclei* 358 (1997), pp. 139–143.

[3] S. Paschalis, I.Y. Lee, A.O. Macchiavelli, et al. "The performance of the Gamma-Ray Energy Tracking In-beam Nuclear Array GRETINA". In: *Nuclear Instruments and Methods in Physics Research Section A: Accelerators, Spectrometers, Detectors and Associated Equipment* 709 (2013), pp. 44–55.

[4] S. Akkoyun, A. Algora, B. Alikhani, et al. "AGATA - Advanced GAmma Tracking Array". In: *Nuclear Instruments and Methods in Physics Research A* 668 (2012), pp. 26–58.

[5] *Advanced GAmma Tracking Array (AGATA) - official website*. URL: `https://www.agata.org`.

[6] A. Gadea, E. Farnea, J.J. Valiente-Dobon, et al. "Conceptual design and infrastructure for the installation of the first AGATA sub-array at LNL". In: *Nuclear Instruments and Methods in Physics Research Section A* 654 (2011), pp. 88–96.

[7] N. Lalović, C. Louchart, C. Michelagnoli, et al. "Performance of the AGATA gamma-ray spectrometer in the PreSPEC set-up at GSI". In: *Nuclear Instruments and Methods in Physics Research Section A: Accelerators, Spectrometers, Detectors and Associated Equipment* 806 (2016), pp. 258–266.

[8] M. Assié, E. Clément, A. Lemasson, et al. "The MUGAST-AGATA-VAMOS campaign: Set-up and performances". In: *Nuclear Instruments and Methods in Physics Research A* 1014 (2021), p. 165743.

[9] *Istituto Nazionale di Fisica Nucleare (INFN) - Laboratori Nazionali di Legnaro (LNL) - official website*. URL: `https://www.lnl.infn.it`.

[10] A. M. Stefanini, L. Corradi, G. Maron, et al. "The heavy ion spectrometer PRISMA". In: *Nuclear Physics A* 701 (2002), pp. 217c–221c.

[11] *PrePAC workshop of the AGATA experimental campaign at LNL*. Nov. 2021. URL: `https://agenda.infn.it/event/26966`.

[12] F. Crespi, F. Galtarossa, J. Pellumaj, M. Rocchini, and M. Sedlak. "Commissioning of AGATA and Complementary Detectors at LNL". In: *Proposal to the LNL PAC* (2022).

[13] K. S. Krane. *Introductory Nucler Physics*. John Wiley & Sons, 1988.

[14] S. Szilner, C. A. Ur, L. Corradi, et al. "Multinucleon transfer reactions in closed-shell nuclei". In: *Physical Review C* 76 (2007).

[15] L. Corradi, G. Pollarolo, and S. Szilner. "Multinucleon transfer processes in heavy-ion reactions". In: *Journal of Physics G: Nuclear and Particle Physics* 36 (2009).

[16] F. Cappuzzello, C. Agodi, D. Carbone, and M. Cavallaro. "The MAGNEX spectrometer: Results and perspectives". In: *The European Physical Journal A* 52.6 (2016).

[17] *Istituto Nazionale di Fisica Nucleare (INFN) - Laboratori Nazionali del Sud (LNS) - official website*. URL: `https://www.lns.infn.it`.

[18] Hervé Savajols. "VAMOS: a VAriable MOde high acceptance Spectrometer for identifying reaction products induced by SPIRAL beams". In: *Nuclear Instruments and Methods in Physics Research B* 204 (2003), pp. 146–153.

[19] *Grand Accélérateur National d'Ions Lourds (GANIL) - official website.* URL: `https://www.ganil-spiral2.eu`.

[20] F. Zardi. *Teoria delle collisioni fra ioni pesanti.* Scuola di Perfezionamento in Fisica dell'Università di Padova, 1979.

[21] A. Winther. "Grazing reactions in collisions between heavy nuclei". In: *Nuclear Physics A* 572 (1994), pp. 191–235.

[22] A. Winther. "Dissipation, polarization and fluctuation in grazing heavy-ion collisions and the boundary to the chaotic regime". In: *Nuclear Physics A* 594 (1995), pp. 203–245.

[23] A. Winther. *GRAZING code website (unpublished).* URL: `http:/www.to.infn.it/%E2%88%BCnanni/grazing`.

[24] S. Szilner, L. Corradi, G. Pollarolo, et al. "Multinucleon transfer processes in $^{40}\mathrm{Ca} + {}^{208}\mathrm{Pb}$". In: *Physical Review C* 71 (2005).

[25] *SRIM - Stopping Power and Range of Ions in Matter.* URL: `http://www.srim.org`.

[26] D. Mengoni, J. J. Valient-Dobón, Farnea. E., et al. "Lifetime measurements of neutron-rich nuclei around ^{48}Ca with the CLARA-PRISMA setup". In: *The European Physical Journal A* 42 (2009).

[27] G. Montagnoli, A.M. Stefanini, M. Trotta, et al. "The large-area micro-channel plate entrance detector of the heavy-ion magnetic spectrometer PRISMA". In: *Nuclear Instruments and Methods in Physics Research A* 547 (2005), pp. 455–463.

[28] S. Beghini, L. Corradi, E. Fioretto, et al. "The focal plane detector of the magnetic spectrometer PRISMA". In: *Nuclear Instruments and Methods in Physics Research A* 551 (2005), pp. 364–374.

[29] M. Rejmund, B. Lecornu, A. Navin, et al. "Performance of the improved larger acceptance spectrometer: VAMOS++". In: *Nuclear Instruments and Methods in Physics Research A* 646.1 (2011), pp. 184–191.

[30] Glenn F. Knoll. *Radiation detection and measurement - 4th edition.* John Wiley & Sons, 2010.

[31] M. Stanley Livingston and H. A. Bethe. "Nuclear Physics C. Nuclear Dynamics, Experimental". In: *Reviews of Modern Physics* 9 (1937), pp. 245–390.

[32] A. Wiens, H. Hess, B. Birkenbach, et al. "The AGATA triple cluster detector". In: *Nuclear Instruments and Methods in Physics Research A* 618 (2010), pp. 223–233.

[33] A. Latina. "Study of Heavy-Ion Reactions with the Magnetic Spectrometer PRISMA: On-line and Off-line Data Analysis". PhD thesis. Università degli Studi di Torino, 2005.

[34] F. Angelini. "Commissioning of the AGATA gamma-ray tracking array". MA thesis. Università degli Studi di Padova, 2022.

[35] *ROOT - A Data Analysis Framework.* URL: `https://root.cern`.

[36] R. Venturelli and D. Bazzacco. "Adaptive Grid Search as Pulse Shape Analysis Algorithm for γ-Tracking and Results". In: *LNL Annual Report 2004* (2005).

[37] A. Lopez-Martens, K. Hauschild, A. Korichi, J. Roccaz, and J-P. Thibaud. "γ-ray tracking algorithms: a comparison". In: *Nuclear Instruments and Methods A* 533 (2004), pp. 454–466.

[38] T. Mijiatović. "Study of heavy-ion reactions with large solid angle magnetic spectrometers". PhD thesis. University of Zagreb, 2015.

[39] *LISE++ - Rare Isotope Beam Production.* URL: `https://lise.nscl.msu.edu/lise.html`.

[40] *NNDC - National Nuclear Data Center.* URL: `https://www.nndc.bnl.gov`.